New methods for electron tomography

Nieuwe methoden voor de elektronentomografie

(met een samenvatting in het Nederlands)

Proefschrift

ter verkrijging van de graad van doctor
aan de Universiteit Utrecht
op gezag van de Rector Magnificus, Prof. Dr. W. H. Gispen
ingevolge het
besluit van het College voor Promoties
in het openbaar te verdedigen
op donderdag 19 december 2002
des middags te 12:45 uur

door

Ulrike Ziese

Geboren op 18 september 1966 te Dortmund (Duitsland)

Promotor

Prof. Dr. A. J. Verkleij
verbonden aan de vakgroep Moleculaire Celbiologie, Universiteit Utrecht

Co-promotor

Dr. Ir. A. J. Koster
verbonden aan de vakgroep Moleculaire Celbiologie, Universiteit Utrecht

The research described in this thesis was performed at the Department of Molecular Cell Biology, Faculty of Biology, Utrecht University, The Netherlands, and was supported by the Royal Netherlands Academy of Arts and Sciences (KNAW, Koninklijke Nederlandse Akademie van Wetenschappen).

Contents

Chapter 1

General introduction

Electron tomography is a method for obtaining three-dimensional (3D) structural information from electron micrographs. It can be applied to a wide range of samples that can be prepared for transmission electron microscopy (TEM)—may they be of biological origin like e.g. cryo or thin plastic sections of cells and tissue or of material science origin like solid catalysts and electronic devices.

A strong advantage of electron tomography is that it does not depend on averaging over unit cells or particles or on the assumption and exploitation of symmetry in samples, as is the case for methods like angular reconstitution (electron microscopy), nuclear magnetic resonance spectroscopy (NMR), electron and X-ray crystallography. Electron tomography can thus be applied to truly unique structures—the only restriction being that the registered image contrast in the electron micrograph must be a projection of some physical characteristic of the sample, e.g. its mass/electron density. This projection requirement implies that, besides conventional bright-field transmission electron microscopy, also energy filtering (zero-loss or element specific) or high angular annular dark-field (HAADF) scanning transmission electron microscopy (STEM) can be utilized in electron tomography.

Electron tomography data acquisition can be regarded as a kind of super-stereology. Instead of images taken from only two different vantage points, a tomographic data set might consist of more than 151 images taken over an angular range of 150°. The more images, and the larger the angular range, the higher the resolution will be within a 3D reconstruction. A rule-of-thumb for the achievable resolution equals three times the thickness of the sample divided by the number of images (for detailed calculations see Radermacher, 1992). Thus for a 300 nm thick sample the resolution would correspond to 6 nm for the 151 images. Though the theory for the 3D reconstruction from projections (weighted back-projection, inverse radon transform) is available for almost a century (Radon, 1917), and the first applications to electron micrographs were published some 30 years ago (DeRosier and Klug, 1968),

the technical burden connected with the acquisition of so many images, each preceded by the rotation of the sample holder and the re-centering and re-focusing of the feature of interest, prevented the application of the technique as a routine tool for 3D structural investigations in the nm-resolution range. One of the reasons electron tomography gained pace during the last decade (Dierksen et al., 1992; Koster et al., 1992) was based on the availability of slow-scan CCD cameras for image acquisition, fast computer systems for on-line image processing and computer controllable electron microscopes. With these instrumental elements available, automated systems for electron tomography data acquisition could be developed—making the method even suitable for the investigation of extremely beam sensitive samples like preparations of frozen-hydrated material (Dierksen et al., 1993 and 1995).

In spite of the fact that the automation efforts in the nineties enabled the application of electron tomography to a variety of samples suitable for transmission electron microscopy, the amount of time and expertise needed for the acquisition of a tilt series discouraged the majority of potential users from routine usage. In chapter 2 we describe a method for automated electron tomography data collection that reduces acquisition time by a factor of five, enabling data collection in less than an hour (Ziese et al, 2002). The method includes a pre-calibration step—measurement and correction of image shift and defocus change at low magnification to detect displacements that might be as large as several μm—before image acquisition. This step avoids switching back and forth between high and low magnification during image acquisition, which is a very time consuming step regarding the electron magnetic lens stabilizations needed. The method is based on the fact that these dislocations occur due to a displacement of the feature of interest from the eucentric height, a displacement of the optical axis from the tilt axis and some movements intrinsic to the sample holder/stage combination and are thus almost predictable.

Pre-calibration electron tomography has been used as an approved method for routine data acquisition in our laboratory for the last two years and has been adapted by several commercial suppliers of software for automated tomography (Emispec, Inc., Tempe, AZ; FEI Co., Eindhoven, The Netherlands; TVIPS, GmbH, Gauting, Germany) in the meantime. The addendum to chapter 2 exemplifies the application of the method with a material science and a biological sample. The first example

shows that the 3D structural investigaton of zeolites, key catalytic materials in applications such as hydro-isomerization of alkanes and hydrocracking of heavy petroleum fractions, can lead to a better understanding of the catalytic activity and selectivity of these materials. The second example illustrates by the 3D study of the Golgi complex that electron tomography of high-pressure frozen and freeze-substituted sections of cell organelles can aid in investigations in cell dynamics and proteomics.

In chapter 3 we discuss a method for the correction of autofocusing errors due to specimen tilt (Ziese et al., 2002c), as this would disable accurate defocus prediction in e.g. pre-calibration tomography. Defocus determination using the beam-tilt method can be hampered for low magnifications and high-tilt angles due to a defocus ramp in the images. The method for the correct cross-correlation (XCF) of two images of a tilted sample acquired under tilted-beam conditions is a modification of the cosine stretch used in the alignment of images acquired under different tilt angles.

As mentioned before, electron tomography is not restricted to the use of transmission electron microscopy. Image acquisition in HAADF-STEM mode makes the method readily available for e.g. crystalline samples, which cannot be acquired in TEM mode as they show angle dependent diffraction contrast. As it was shown that nm-sized inclusions in crystalline material can be detected by this method (Midgely et al, 2001) we have applied the approach to the detection of ultrasmall immuno-gold labels absorbed to heavy-metal stained plastic sections of biological material. Our initial experiments discussed in chapter 4 (Ziese et al., 2002b) provide good evidence that HAADF-STEM electron tomography could be a useful tool for the accurate 3D immuno-localization of proteins. So far the method is time consuming as all images were acquired by manual operation of the STEM, but we assume that pre-calibration will be applicable in automation and thus provide routine application of STEM tomography.

Finally, chapter 5 discusses our work in the context of recent trends in automation and application of electron tomography.

Chapter 2

Automated high-throughput electron tomography by pre-calibration of image shifts

ULRIKE ZIESE, ANDRIES H. JANSSEN, JEAN-LUC MURK, WILLIE J.C. GEERTS, THEO P. VAN DER KRIFT, ARIE J. VERKLEIJ & ABRAHAM J. KOSTER

Summary

Electron tomography is a versatile method for obtaining three-dimensional (3D) images with transmission electron microscopy (TEM). The technique is suitable to investigate cell organelles and tissue sections (100–500 nm thick) with 4–20 nm resolution. 3D reconstructions are obtained by processing a series of images acquired with the samples tilted over different angles. While tilting the sample, image shifts and defocus changes of several μm can occur. The current generation of automated acquisition software detects and corrects for these changes with a procedure that incorporates switching the electron optical magnification. We developed a novel method for data collection based on the measurement of shifts prior to data acquisition, which results in a five-fold increase in speed, enabling the acquisition of 151 images in less than 20 min. The method will enhance the quality of a tilt series by minimizing the amount of required focus-change compensation by aligning the optical axis to the tilt axis of the specimen stage. The alignment is achieved by invoking an amount of image shift as deduced from the mathematical model describing the effect of specimen tilt. As examples for the application in biological and materials sciences 3D reconstructions of a mitochondrion and a zeolite crystal are presented.

Journal of Microscopy, Vol. 205, Pt 2 February 2002, pp. 187-200.

Introduction

Electron tomography is a technique for imaging relatively large (100–500 nm) variable structures (e.g. cell organelles, whole cells, tissue sections) in 3D with moderate to high resolution (4–20 nm) (Frank, 1992 and 1995; Koster et al., 1997; Baumeister et al., 1999; McEwen and Marko, 2001). In contrast to stereo-microscopy, where two tilted electron microscope recordings are used for 3D analysis of microscope specimens (Starink et al., 1995), with electron tomography TEM images of a specimen tilted over different tilt angles (a tilt series) are combined to compute a 3D image (reconstruction) of the specimen density. Inherent to the approach are two key assumptions: (1) that the TEM images are in good approximation 2D projections of the mass density of the imaged sample; and (2) that the specimen does not change during data collection.

In spite of the early recognition of electron tomography as a high-resolution 3D imaging tool (Hart, 1968; Hoppe et al., 1968; Crowther et al., 1970; DeRosier and Klug, 1968), routine application of the technique has been prevented by considerable technical obstacles during the last few decades. A major problem lay in reconciling two conflicting requirements of the technique. To obtain a high-resolution (detailed) 3D reconstruction, a tilt series must be recorded that covers as wide an angular tilt interval as possible (to minimize the missing amount of information) with tilt increments as small as possible (to maximize the resolution by fine angular sampling) (McEwen and Marko, 1999; Baumeister and Steven, 2000). At the same time, the specimen must not change during data collection and, consequently, the electron dose used to record a tilt series must be as low as possible (Grimm et al., 1998).

Early on, a solution to these contradicting requirements was proposed: to partition a fixed amount of (allowable) electron dose over the number of projections that are required to attain a certain (desirable) resolution (Hegerl and Hoppe, 1976; McEwen et al., 1995). Although low-dose imaging techniques can be carried out to distribute the allowable dose over the number of images, practical problems are aggravated due to the fact that when a specimen holder is tilted, image shifts and defocus changes of several μm can occur while tilting the sample. Therefore, the acquisition of more than a hundred images with 1° tilt increment is a demanding task as defocus changes and

image shifts need to be corrected after every tilt increment. As a consequence, the application of high-resolution electron tomography remained restricted to a limited group of practitioners of the technique.

During the last decade, the application of electron tomography has gained pace. With the advent of computer-controlled microscopes, large-scale digital cameras and high-performance desktop computing power, it became possible to implement automated procedures for the acquisition of tilt series containing hundreds of views that are recorded under very low-dose conditions (Dierksen et al., 1992, 1993, 1995; Koster et al., 1992; Braunfeld et al., 1994; Grimm et al., 1997; Koster et al., 1997; Rath et al., 1997; Dierksen et al., 1995). Simultaneously, several computer program packages for alignment, reconstruction and manipulation of large volumetric data sets matured and became available to the scientific community (Frank et al., 1996; Fung et al., 1996; van Heel et al., 1996; Kremer et al., 1996; Schroeter et al., 1996; Hegerl and Altbauer, 1982).

With automated data collection several problems that limited the practical application of electron tomography are overcome. Automated tomography enables the image acquisition with a (digital) CCD camera, which implies that changes in image position and defocus can be detected by on-line image processing and immediately be corrected for by computer control of the microscope. In addition, the tilt series are directly available in digital format for subsequent processing and reconstruction. Typically, carrying out an electron tomography experiment with the first generation of automated systems will take a day, and the actual data collection 2–4 hours (Koster et al., 1997).

In this article we discuss the possibilities and the implementation of a second generation automated data collection procedure that significantly increases data collection speed and widens the applicability of the technique. The basic idea of the novel method is that the image movement is calibrated prior to data collection. The movement of the stage is measured both in the *xy*-plane (image shifts) and the *z*-direction (defocus change) for the range of tilt angles needed to acquire a tilt series. It appears to be sufficient to record these measurements at low magnification with 5° tilt increments and to interpolate the values of image shift and defocus change in between when the actual data set is acquired with smaller tilt increments

and at higher magnifications. In addition, it also appears possible to model the observations of image shifts and focus changes. Using the mathematical model it becomes possible to predict the overall image movements after a few measurements of image shift and defocus change. It is also possible to create novel strategies in collecting tilt series to optimize data collection to specific requirements such as the desired field of view, resolution or electron dose.

The pre-calibration data acquisition approach shows a substantial increase —five-fold—in data collection speed compared to the first generation of automated data acquisition methods. One of the reasons for this increase in speed is that, in contrast to the first generation of automated systems, it is not required to switch the electron optical magnification of the TEM back and forth during data collection.

The pre-calibration approach will also enhance the quality of a tilt series if the amount of required focus-change compensation during data acquisition is minimized by aligning the optical axis to the tilt axis of the specimen stage. The alignment is achieved by invoking an amount of image shift as deduced from the mathematical model describing the effect of specimen tilt.

Another advantage of the pre-calibration approach is that the required computer-controlled steps for tracking image shifts and defocus changes are uncoupled from the acquisition of the tilt series. The uncoupling provides possibilities for acquisition modes other than bright-field imaging and provides opportunities to use detectors other than CCD/film. For instance, a tilt series can be taken in STEM mode (Beorchia et al., 1993; Midgley et al, 2001) and, simultaneously, (3D) element-specific information of the sample could be collected with an energy dispersive X-ray (EDX) detector. Especially for applications in the field of materials sciences, which just recently started to apply the technique (Koster et al., 2000; Janssen et al., 2001), as well as for automated procedures to localize in 3D high-density labels within a specimen, 3D elemental map information could be very useful.

We evaluated the pre-calibration method under different stage and imaging conditions. A model describing the overall image movement when tilting the stage is derived and the reliability of determining relative shifts is shown to be 10 nm. In addition, we describe the current software implementation and present 3D

reconstructions obtained by the methodology in the fields of both biological and materials sciences.

Materials

Experiments were performed on a 200-kV Tecnai 20 (S) transmission electron microscope (FEI/Philips Electron Optics, Eindhoven, The Netherlands) at a nominal magnification of 5000× (screen up) and a defocus of –10 μm. The Tecnai PC is equipped with a dual 350 MHz Pentium II processor, which contains 512 Mb of RAM and 4 Gb of disk space. Images were recorded with a bottom-mounted slow-scan CCD camera (TemCam F214, Tietz Video and Image Processing Systems GmbH, Gauting, Germany). The post-magnification factor from the film-plane to the CCD chip is 1.8×. The CCD array is composed of 2048 × 2048 square pixels of 14 μm. At a magnification of 5000× the images represented a specimen area of 3186 nm × 3186 nm. For the experiments, images of 512 × 512 pixels with 6.2 nm/pixel were collected (binning 4). The readout rate of the CCD images is 2 Mb/s (12 bits/pixel). The replica of a 2160 lines/mm waffle-pattern diffraction grating (Electron Microscopy Sciences, Washington, PA) was used as a calibration standard and tilted from –60° to +50°/55° and vice versa either in a FEI/Philips standard specimen holder or a Gatan model 670 ultra-high-tilt holder.

Automation procedures for calibration of image shift and autofocus, and detection of these shifts and changes, were implemented in JavaScript as a component (macro) in TIA (Tecnai Imaging and Analysis, Emispec Systems Inc., Tempe, AZ). TIA is an addition to the Tecnai software, interfacing with detectors on the microscope (e.g. CCD camera, STEM detector). At every tilt angle CCD images of the sample were recorded to detect image shifts and defocus changes. Image shifts were measured by cross-correlating images acquired before and after a specimen tilt increment. Defocus changes were measured using the beam-tilt method (Koster et al., 1987 and 1989). The beam-tilt method makes use of the fact that an image shift will occur when the illuminating beam is tilted and the microscope is not in focus. The amount of image shift is linearly related to the amount of defocus.

Off-line image processing has been carried out on a UNIX workstation (Octane dual-processor 2 × 250 MHz R10000 (IP30), Silicon Graphics Inc., Mountain View, CA). The IMOD program (Kremer et al., 1996) was used for the detection of the specimen-tilt axis, image alignment and 3D reconstruction. The IVE program (Fung et al., 1996) was used for general 3D volume handling and processing. The Huygens and FluVR programs (Scientific Volume Imaging BV, Hilversum, The Netherlands) for visualization. Modeling computations were carried out on a Windows 98 PC (Microsoft Inc., Redmond, WA) with the program Excel (Microsoft Inc.).

Methods and Results

A. Acquisition of a stage calibration curve

The magnification of the microscope was calibrated with a cross-grating and the proper functioning and accuracy of the computer-control procedures for determining and correcting image shifts and focus changes were determined once before the whole study.

Stage calibration curves were acquired by measuring specimen movement (i.e. image shifts in the *xy*-plane and defocus changes in the *z*-direction) as a function of specimen tilt.

1. First, to ensure proper cross-correlation between images recorded before and after an induced specimen tilt, an imperfection (a specific, non-repeating) feature on the cross-grating grid was selected.
2. Next, the sample was set manually to eucentric height.
3. The sample was tilted to its initial tilt angle.
4. The initial ImageBeamShift and/or the *z*-height of the specimen relative to the manually chosen eucentric height were varied in the range +3 µm to –3 µm for testing different experimental situations.
5. The image was defocused to –10 µm (automatically).

6. The feature on the cross-grating was centered on the CCD camera image using the image-shift coils (automated).

7. To minimize mechanical hysteresis effects, and therefore minimize initial image shifts, a tilt angle setting was always approached from the same direction. For instance, if the initial tilt angle was −60°, the stage was first set to −62° and then back to −60° to make sure that even the first tilt angle in the measurement was approached from the negative side. The image feature was then automatically re-centered and re-focused.

8. Next, change of tilt angle. The tilt increment was ±5°.

9. Detection of defocus change using the beam-tilt method. With the beam-tilt method the position of the maximum value (i.e. peak) after cross-correlating images recorded with '+' and '–' beam tilt is a direct measure of defocus. Defocus change was only measured, not corrected for.

10. Detection and correction of image shifts. Image shift was measured by cross-correlating two images before and after specimen tilt. The centering of the feature provided an immediate feedback to the operator if the detected shifts and compensations were carried out correctly.

11. The absolute image shifts and defocus changes that occurred relative to the conditions of the first tilt angle were calculated and saved to a file.

12. The measurements as listed in steps 8–11 were repeated until the final tilt angle was reached.

B. Model for stage calibration curves

The actual shape of the acquired calibration curve depends on:

- a displacement of the tilt axis of the goniometer from the optical axis;
- the fact that the specimen holder was removed/inserted;
- the *x*/*y* of the stage position;
- an *x*/*y*/*z* change in stage position;
- the *z*-height of an image feature;
- image-shift settings.

Only the last two parameters can be adjusted by the user, who is interested in an image feature at a certain stage position. Note, however, that the first parameter (the displacement of the tilt axis of the goniometer from the optical axis) is influenced by the last parameter (the image-shift settings). Fig. 1 shows *x*- and *z*-calibration curves acquired at a single stage position under different *z*-height and image-shift settings. With the best settings (Fig. 1E) there will be hardly any shifts; otherwise shifts can be positive or negative and can take values up to several µm.

We postulate that all observed calibration curves can be explained by modeling the specimen tilt as a rotation of a rigid body around an axis *A* of the coordinate system (Fig. 2). A difference of just 2° between the tilt axis (i.e. the direction along the specimen holder) and the *y*-axis of the CCD images was determined from the images subsequently acquired during the calibration measurements. Therefore, the tilt axis could be identified to a good approximation with the *y*-axis. At 0° tilt the sample point *P* has coordinates x_0, y_0 and z_0. When the sample is tilted by α the new coordinates will be:

$$x(\alpha, x_0, y_0, z_0) = z_0 * \sin(\alpha) + x_0 * \cos(\alpha)$$

$$y(\alpha, x_0, y_0, z_0) = y_0$$

$$z(\alpha, x_0, y_0, z_0) = z_0 * \cos(\alpha) - x_0 * \sin(\alpha) \qquad (1)$$

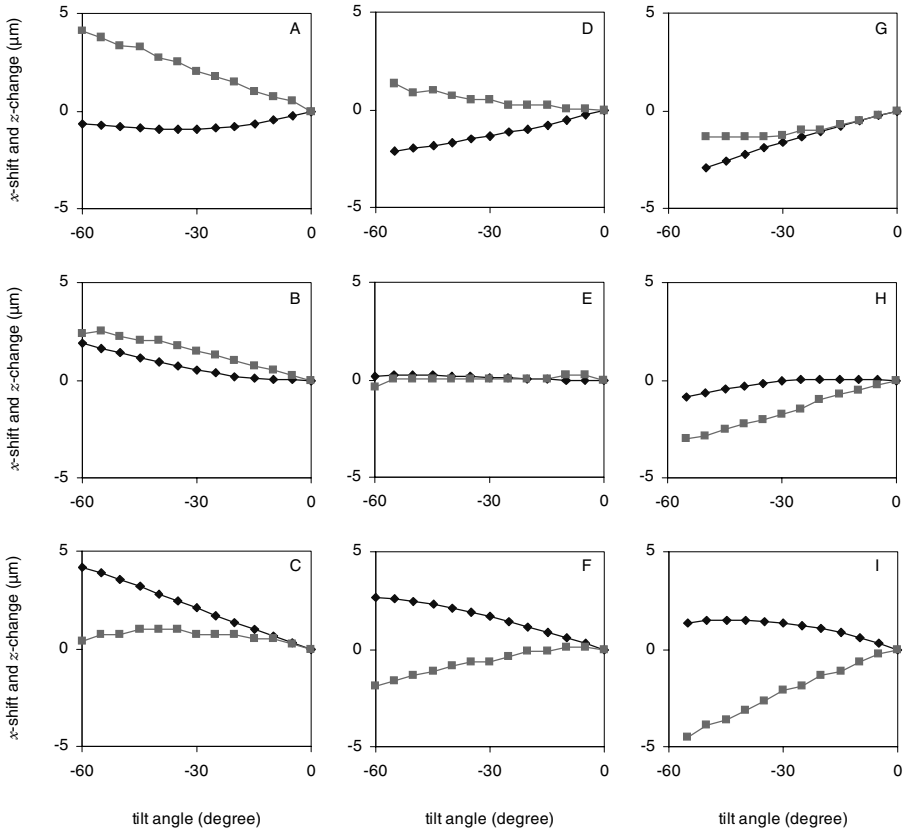

Fig. 1. Absolute x-image shifts (◆) and defocus changes (■) that an image feature undergoes after the sample is tilted to a certain angle (0°–60°), under various image-shift and z-height settings at a single stage position. From left to right the initial image shift and from bottom to top the z-height was varied from about –3 µm to +3 µm.

So, the measured image shifts correspond to the changes in the x- and y-coordinates and the defocus change corresponds to the change in the z-coordinate. The parameter z_0 can be identified as the z-height of the feature of interest and x_0 describes a composite effect of the other influences that displace the center of rotation

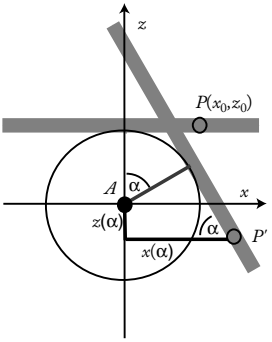

Fig. 2. Spatial coordinates of a sample point P (image feature) before (x_0, z_0) and after rotation/ tilting of a ($x(a)$, $z(a)$) around the y-axis of the coordinate system.

from the optical axis. x_0 can take values of up to several µm even if the image shift was set to zero before starting the experiment.

C. Least-squares fitting of calibration curves

For showing that the measured image shifts and defocus changes in a TEM actually describe a rotation of the image feature around the y-axis of the image, we have applied statistical parameter estimation techniques to two sets of calibration curves.

The first set corresponds to a situation were x_0 is close to zero (recorded at stage position x = 3.49 µm, y = –12.48 µm); in the second set x_0 was about 9 µm (x = –198.47 µm, y = 11.03 µm; Fig. 3). Before taking each data set the sample was set to eucentricity. In one set the z-height of the holder was varied from eucentricity +3 µm to eucentricity –3 µm, in the other from +3 µm to –4 µm (both with increments of 1 µm). Note especially the large change in defocus for the second data set. We could not find a direct connection between stage position and difference in the x_0 parameter and we conclude that the difference was mainly due to the (unregistered) initial image-shift settings. Therefore pre-calibration curves acquired for a certain stage position cannot be applied directly to the acquisition of a tilt series at another stage position if the initial image-shift settings are not identical.

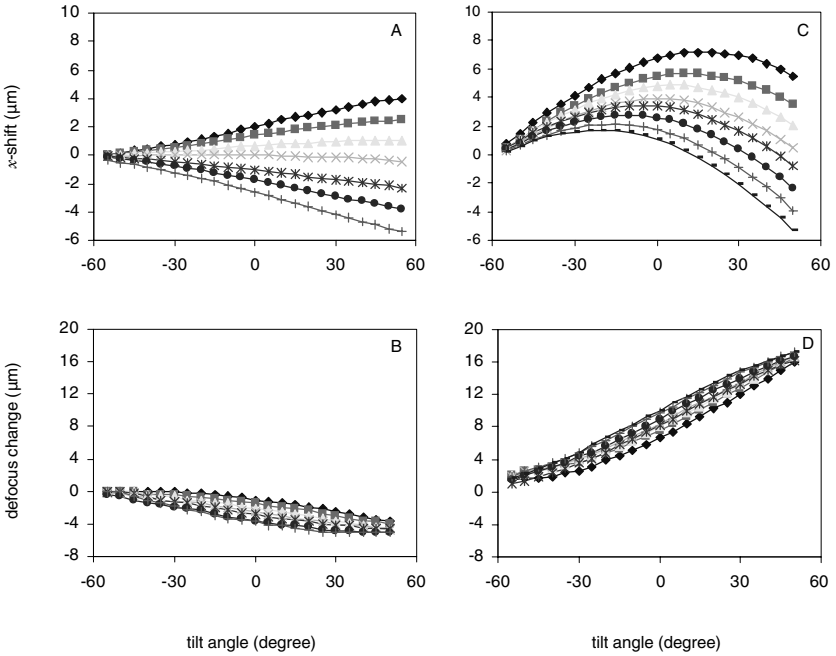

Fig. 3. Calibration curves acquired from –60° to +50° at two stage positions. (A) and (C) are absolute x-image shifts, (B) and (D) are absolute defocus changes. The left set corresponds to a situation were x_0 is close to zero (recorded at stage position x = 3.49, y = –12.48 µm), in the right set x_0 was about 9 µm (x = –198.47, y = 11.03 µm). Each set consists of several curves that were recorded with different z-height settings of the goniometer. The nominal values from top to bottom as indicated by the Tecnai user interface were z = 2.98, 1.97, 0.98, 0.02, –0.94, –1.94, –2.96 (left) and z = 2.98, 2.07, 1.04, 0.05, –0.94, –1.94, –2.95, –3.93 (right) µm.

A least squares fit to the modelled image movement can be found with:

$$\text{measurement}(a, x_0, z_0) = x_0 * \cos(a) + z_0 * \sin(a) + c \qquad (2)$$

$$\begin{pmatrix} x_0 \\ z_0 \\ c \end{pmatrix} = \begin{pmatrix} \sum \cos(a)^2 & \sum \sin(a)\cos(a) & \sum \cos(a) \\ \sum \sin(a)\cos(a) & \sum \sin(a)^2 & \sum \sin(a) \\ \sum \cos(a) & \sum \sin(a) & \textit{number measurements} \end{pmatrix}^{-1} * \begin{pmatrix} \sum \cos(a)\,\textit{measurement} \\ \sum \sin(a)\,\textit{measurement} \\ \sum \textit{measurement} \end{pmatrix}$$

Table 1

		Data set one	Data set two
Estimates (µm) from all data	x_0	0.08, 0.18, 0.25, 0.48, 0.40, 0.46, 0.54	8.98, 8.67, 8.79, 8.71, 8.98, 9.01, 9.03, 9.16
	z_0	2.43, 1.54, 0.7, -0.17, -1.28, -2.20, -3.03	2.71, 1.62, 0.7, -0.22, -1.12, -2.01, -2.91, -3.82
Estimates (µm) from 3 points	x_0	0.09, 0.35, 0.40, 0.70, 0.51, 0.63, 0.84	9.20, 9.13, 9.25, 9.27, 9.32, 9.52, 9.64, 9.76
	z_0	2.47, 1.58, 0.73, -0.14, -1.25, -2.15, -2.97	2.78, 1.72, 0.80, -0.12, -1.04, -1.89, -2.80, -3.70

Table 1 shows the parameters that were calculated from the measured *x*-shifts for the first and second data set. Note that the value for x_0 was found to vary slightly between measurements at different *z*-heights.

Substituting the estimated values of x_0 and z_0 in the mathematical model, we can compute the difference between the measured curves and the estimated curves. As differences are small, we have displayed the relative shifts (changes between images of successive tilt angles) rather than the absolute *x*-shifts. Fig. 4 shows the measured data (top), the modelled data (middle) and the difference (bottom) for the two data sets. Note that the difference is just in the order of tens of nm, indicating that the stage does rotate in a predictable manner and that the movement is highly accurate. The difference is probably caused mainly by the characteristic properties of the stage.

The statistical estimation of parameters can be exploited in different ways. When an estimate of the parameters (the distance from eucentric height, the initial image shift) has been performed after a first measurement, it would be possible to adapt those parameters on the microscope. The goal would be that less image movement and less focus change will occur when the specimen is tilted.

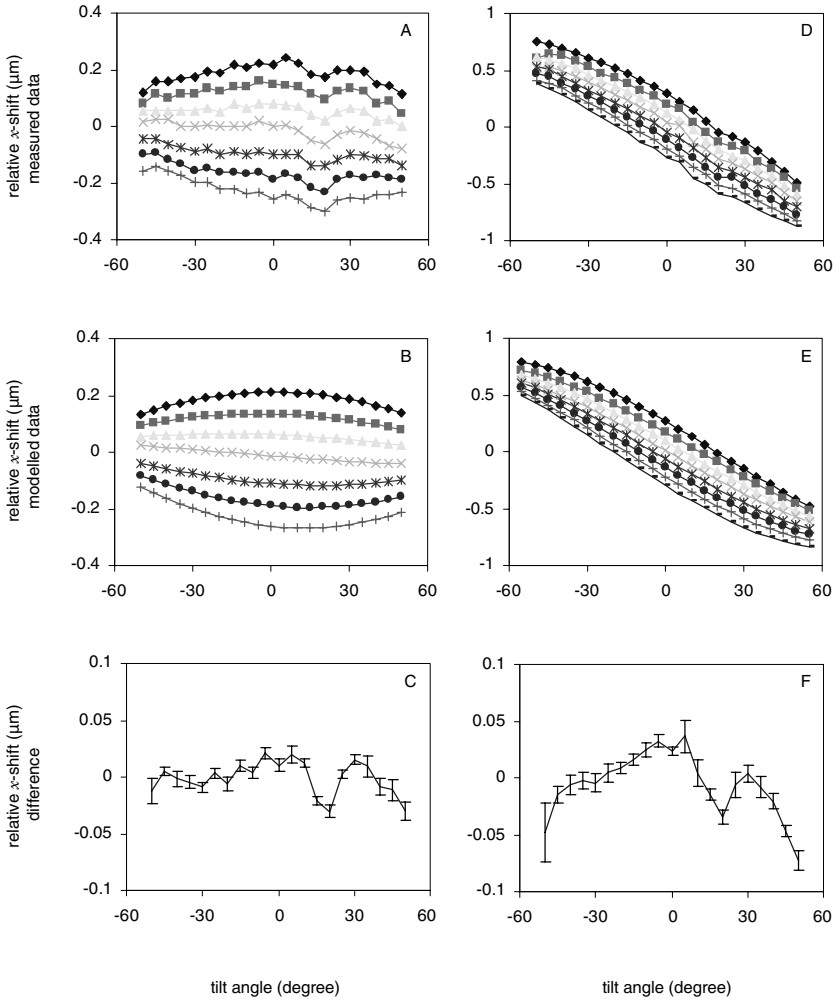

Fig. 4. (A) and (D) Relative x-image shifts between tilt angles, extracted from the curves shown in Fig. 3. (B) and (E) Relative shifts, calculated from a mathematical model whose parameters were given by least squares fitting of the measurement. (C) and (F) Mean value and standard deviation of differences between measured and modelled data.

Finally, as it was shown, the parameters x_0 and z_0 can even be estimated quite well from just three measurements. When we define $\Delta x(+\alpha)$ as the x-shift occurring between angles $+\alpha$ and 0° and $\Delta x(-\alpha)$ the x-shift between angles $-\alpha$ and 0°, then x_0 and z_0 can be calculated from:

$$x(-\alpha, x_0, z_0) = z_0 * \sin(-\alpha) + x_0 * \cos(-\alpha) \quad (3)$$

$$x(0, x_0, z_0) = x_0$$

$$x(+\alpha, x_0, z_0) = z_0 * \sin(+\alpha) + x_0 * \cos(+\alpha)$$

$$\Delta x(-\alpha) = x(0, x_0, z_0) - x(-\alpha, x_0, z_0)$$

$$\Delta x(+\alpha) = x(0, x_0, z_0) - x(+\alpha, x_0, z_0)$$

$$x_0 = 0.5 / (1 - \cos(\alpha)) * (\Delta x(-\alpha) + \Delta x(+\alpha)) \quad (4)$$

$$z_0 = 0.5 / \sin(\alpha) * (\Delta x(-\alpha) - \Delta x(+\alpha))$$

Table 1 shows the values that were calculated from the measured image shifts between 0°and ±30° for the first and second data set mentioned above.

In principal, the parameters x_0 and z_0 can also be calculated from the defocus changes and in the general case, where the tilt axis is not identical to the y-axis, image shifts and defocus changes have to be used simultaneously to find the best fit to the measurement.

The model of the sample movement can further be used to predict the maximal image shift and can indicate up to what magnification the approach can be used. To ensure that a shift between images acquired before and after a tilt increment can be measured, the magnification has to be chosen such that the image size is four times (at best) larger than the shift to be measured. The maximal image shift for x_0=10 µm (corresponding to the curves with the largest shifts measured) for a tilt series starting at −70° and tilt-angle increments of 5/1° is 0.8/0.16 µm for z_0=0 µm . For z_0=3 µm the maximal shift is 0.9/0.18 µm.

Table 2

Magnification (kx) screen up	Image size (μm) CCD camera
5	3.19
11.5	1.39
19	0.84
29	0.33

Table 2 shows the CCD image size at different magnifications (2048 × 2048 CCD pixels of 14 μm and post-magnification factor 1.8×). The values show that when the *z*-height of the sample is kept within 3 μm of eucentricity, pre-calibration curves with a tilt-angle increment of 5° can be acquired up to a magnification of 5000×. According to the mathematical model it would not be necessary to acquire a pre-calibration curve up to a magnification of 19000× because the maximal *x*-shifts could still be detected at that magnification provided that the tilt increment is not larger than 1°.

D. Reproducibility of calibration curves

It has been shown that the movement and defocus change that an image feature undergoes while being tilted from one angle to another can be explained by a simple rotation and that consequently the displacement of the image feature from the center of the rotation in *x*- and *z*-directions can be determined and corrected for from these changes.

The applicability of this approach is closely related to the accuracy that is expected of the pre-calibration method. This depends on the envisioned magnification and if the aim is to use the method merely to avoid having to determine the shifts at low magnification or to avoid any measurements at the acquisition magnification during data acquisition.

To determine the fine structure and reproducibility of calibration curves, measurements were performed without initial image shift and close to eucentricity.

Eight measurements were recorded at a single stage position, four with increasing and four with decreasing tilt-angle increment for the normal and high-tilt holder (Fig. 5). x_0 and z_0 values were calculated from the measurements but have to be taken with care, because least squares fitting becomes less meaningful as the additional shifts due to unique stage characteristics reach the same order of magnitude as that imposed by the rotational movement.

For the tilt direction with increasing angles x_0 values of 0.9 and 0.8 μm were calculated for both the standard and high-tilt holder. This indicates that the displacement of the center of rotation is about 1 μm for the two holders tested and thus probably the accuracy to which the stage was assembled. z_0 has been determined to 0 and 0.2 μm. As already noticed during other measurements, the same parameters calculated from the defocus changes yielded slightly different values, 1.8 and 1.1 μm for x_0 and 0.9 and 0.5 μm for z_0. Thus the z-change of an image feature seems to follow a rotation around a slightly different center. This implies furthermore that either image x-shift or defocus change could be minimized by accordingly adjusting initial image shift and z-height. During further experiments it was shown that by doing so the maximal relative and absolute x-image shift could be reduced to about 20 and 200 nm, respectively, while the absolute defocus change still reached 2 μm.

Fig. 5 displays the relative shifts of the 16 measurements. The relative shifts in x-direction were less than 100 nm and would have been even smaller if x_0 had been corrected before the measurement. The deviation in values was 10 nm, indicating to what accuracy the pre-calibration curves could be applied during the final tilt series for image acquisition. The similarity of the curves for the normal and high-tilt holders further implies that the shifts are a characteristic of the stage rather than of the holders. The difference in these curves could be ascribed to slightly different values in x_0 and z_0—the particular loading of the holder into the stage—rather than to the holders themselves. Possibly, one could extract the stage characteristics to avoid the necessity for any pre-calibration measurement.

Relative image y-shifts are generally insignificant (also error bars were too small to show), except for a sudden jump of 100 nm at 15° tilt angle (increasing tilt angles) or 0° (decreasing tilt angles). Note that this increase happens in the same y-direction for

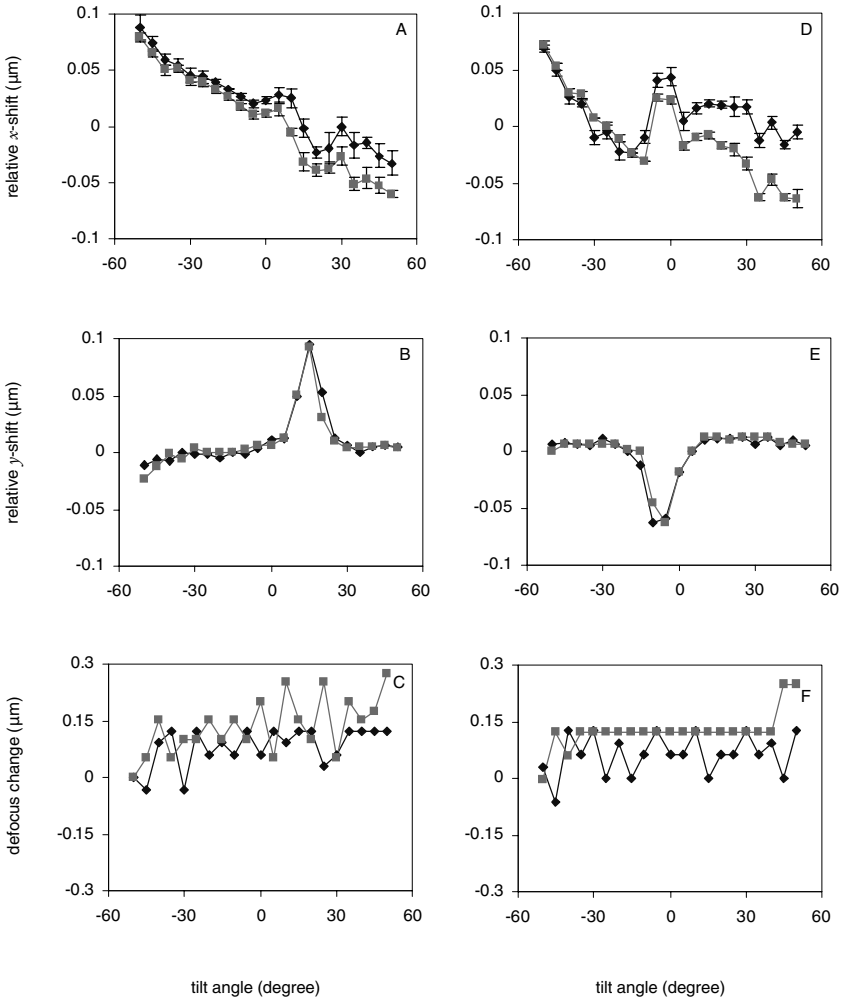

Fig. 5. Mean value and standard deviation of eight calibration curves recorded with the normal (■) and high-tilt (◆) holder, when the image feature was close to eucentricity and with no initial image shift. The shifts/changes are relative values between tilt angles, which were effectively measured and need to be corrected for. (A)–(C) recorded from –65° to +65° (high-tilt holder) and –60° to +55° (normal holder). (D)–(F) Curves recorded for the same angular range but with opposite tilt direction. Values have been inversed to facilitate comparison.

both tilt directions. Thus there is an absolute displacement of an image feature of about 500 nm after first tilting the sample in one direction and than going back, if these shifts are not corrected. The relative defocus changes vary around 0.1 μm for all measurements. Further conclusions cannot be drawn, as the accuracy of defocus measurement was not better than about 200 nm due to the small magnification.

The overall conclusions from these measurements are that the pre-calibration of image shifts and defocus changes should be applied in two steps. First, to predict and correct x_0 and z_0 at a low magnification from a few measurements. Second, to record the changes in detail to an accuracy of 10 nm (if this accuracy is needed) at the envisioned magnification for data acquisition (mainly to accurately determine defocus changes). The remaining task for the software during the acquisition of a tilt series would possibly be to correct for drift, which may well be present when a cryo-holder is used.

E. Software implementation

The current generation of transmission electron microscopes from FEI/Philips Electron Optics (Tecnai series of TEM) allows a much higher degree of remote control than previous TEM models. This is caused by the fact that the whole logistics of the microscope (e.g. control of currents) are performed by the Temserver, a software program (service) that runs on a PC under the Windows NT operating system (at the time of writing). The procedure for operating the microscope consists of logging in to the PC and starting the Tecnai User Interface, a software program (application) that presents functionality to the microscope operator and that communicates with the Temserver. In addition, the most often accessed microscope functions, such as change of magnification or defocus, are controllable through buttons and knobs on panels left and right of the column. Furthermore, the Windows Scripting Host, which is part of the operating system, can act as a means to glue various programs or components (COM objects) together. The Tecnai User Interface, for instance, is a COM object that communicates with the Temserver. Another one is Tecnai Scripting, which interfaces between scripting languages and the Temserver. This software set-up implies that it is possible to build a separate COM object to control the microscope in some particular manner. For instance,

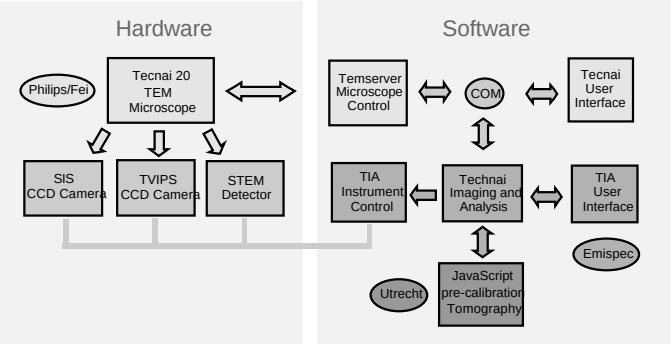

Fig. 6A. Hardware and software set-up utilized in our laboratory to implement pre-calibration electron tomography. Contributions from different parties are displayed in different shades of gray. Our contribution comes in form of a JavaScript program (see label Utrecht).

a few lines of the JavaScript programming language placed in a simple HTML page and viewed with a web browser will be sufficient.

A full-featured tomography data acquisition program has to be able to carry out several functions that are not mere microscope control functions and (so far) not available by the FEI/Philips software. The functions are: control of CCD cameras, display of images, image processing and creation of user interface elements. To have access to this additional functionality, we have chosen to implement tomography as a macro (component) in TIA (Tecnai Imaging and Analysis, Emispec), a program that provides these missing functions. Furthermore, TIA is able to host COM objects and script macros and can thus execute JavaScript programs. We have chosen to write the component in the JavaScript language, widely used and easy to learn. Fig. 6A shows an overview of the software architecture.

A first version of the tomography component for TIA is available for download from our web site (http://www.bio.uu.nl/mcb/3dem > Scripting > OpenTomography > Download the latest JavaScript code). We have named it OpenTomography, indicating that the source code of the software is freely available and with the possibility to modify it. OpenTomography is available under the GNU Public License and is distributed by the 3D EM group at Utrecht University. It contains essential parts for collecting a tilt series on a FEI/Philips Tecnai TEM. The current version was tested at various microscope set-ups, at Utrecht University (a Tecnai 20 LaB_6 with TVIPS 2k × 2k slow-scan CCD camera) and the FEI/Philips research

laboratories (e.g. a Tecnai 12 BioTwin with GIF, a Tecnai 20 FEG with GIF).

In our opinion, the ideal open source code for the further development of electron tomography should be based on as few commercial software components as possible. The code should therefore be as generic as possible to enable the end-user to decide which non-commercial (or commercial) software to use to deliver CCD control, image display and user interface. It is therefore perfectly feasible to imagine a future version of open source code tomography to use a straightforward web page as user interface and a dedicated mathematical package (e.g. MRC libraries) for image processing.

Fig. 6B gives a comparison between the conventional data acquisition approach and the pre-calibration approach. The left-most column shows the timing for the conventional approach. Acquiring a data set will take 103 min, of which 50 are needed for switching the magnification. For the pre-calibration approach, the timing for four different data collection modes is shown. The column second from the left shows the timing when additional focusing and tracking is carried out (for the highest accuracy). The total time will be 60 min: for taking a pre-calibration curve (6 min), for the actual tilt series (18 min) and for the additional focusing and tracking during data collection (36 min). The middle column shows the timing when additional tracking is carried out. The total time will be 36 min: for taking a pre-calibration curve (6 min), for the actual tilt series (18 min) and for the tracking (12 min). The column second from the right shows the timing for taking a tilt series, together with a calibration curve. The total time will be 24 min: for taking a pre-calibration curve (6 min) and for the actual tilt series (18 min). The right-most column shows the timing for taking the tilt series only. The total time will be 18 min, 5.9 times faster than the conventional approach. In the comparison it is assumed that the hardware used to carry out the experiments is identical. A tilt series is supposed to consist of 151 images (with 1° tilt increment) and that 31 images are needed for the calibration curve images (with 5° tilt increments). Furthermore, it is assumed that a magnification switch requires 10 s of idle time before all currents in the lenses are stable and that 3 s are needed before the specimen is sufficiently stable after a specimen tilt-angle increment. Also, it is assumed that 1 s exposure time is required for the images of the tilt series (the data) as well as for the images of microscope control (focusing,

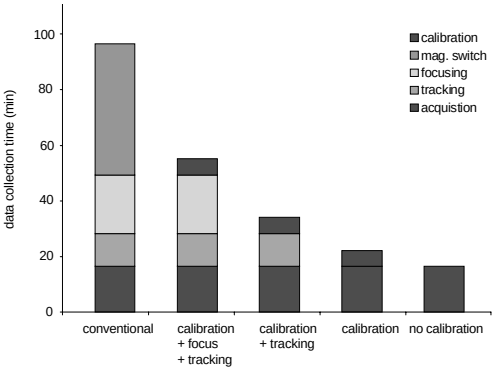

Fig. 6B. Comparison between the conventional data acquisition approach and the pre-calibration approach. Currently, our implementation of pre-calibration tomography acquires a tomographic data series with 151 images in 20 min (current version of software and PC). This is a six-fold increase in the speed of the tracking step compared to the conventional implementation where switching forth and back to a small magnification is necessary to detect large image shifts.

tracking). It is assumed that 3 s are needed to transfer and display each individual image and that a cross-correlation will take 1 s.

F. Example Reconstructions

To illustrate the application of pre-calibration electron tomography we next discuss the reconstruction of two tilt series that were acquired with the described set-up. In these early applications we did not yet fully exploit the potential of the method, but merely took advantage of the possibility to eliminate magnification switches.

As one experiment in a series to elucidate the formation of cavities in zeolite crystals under different preparation methods (Janssen et al., 2001; also see the addendum to this chapter), 151 projections (-75° to +75°) of a crystal were acquired. The understanding of the growth mechanism is important as cavities influence the catalytic activity of zeolite crystals. A slice through the reconstructed volume clearly displays cavities of different sizes in the structure (Fig. 7A). Fig. 7B shows a surface rendered view of the zeolite.

A total of 121 projections (-69° to +51°) of a semi-thick section of high-pressure frozen and freeze-substituted murine dentritic cells were acquired. Slices through a part of the reconstructed volume display the organization of the lamellar compartments of a mitochondrion (Fig. 7C, top *xz*-, bottom *xy*- and right *zy*-slice). Fig. 7D shows a surface rendered view.

Discussion and conclusions

While tilting samples in our Tecnai 20 transmission electron microscope, we measured relative image shifts between images recorded at different tilt angles of up to about 1 µm and absolute image shifts up to about 6 µm for tilt series from –60° to +60°, 5° angle increments and a *z*-position of the specimen holder 3 µm away from eucentricity. The absolute defocus changes reached values up to about 20 µm. This measurement was not done under accurately specified initial image-shift conditions. When no image shift was induced prior to the experiment and for a *z*-position close to eucentricity the relative and absolute image shifts were less than 100 nm and 500 nm, respectively. The shifts can further be decreased to about 20 nm and 200 nm, respectively, by applying a compensating initial image shift. We investigated shifts and defocus changes under different conditions to determine if they can reliably be detected by a pre-calibration measurement. It was shown that the measured calibration curves are different for different distances from eucentricity, different for different imaging conditions (image-shift settings), reproducible to an accuracy of about 10 nm for the relative image *x*-shift between tilt angles if acquired under the same conditions. These observations indicate that changes can reliably be detected by a pre-calibration measurement, but that a pre-calibration measurement cannot be directly used to predict the movements under other (unknown) conditions.

It was also shown that the overall shape of measured calibration curves could be explained mathematically by a rotation of the specimen holder around a fixed axis. This implies that the measured image shifts of an image feature will be the changes in the *x*- and *y*-coordinate and that its defocus change corresponds to the change in the *z*-coordinate. Consequently, the unknown parameters of the movement can be approximated from the image shifts between a few tilt angles by least squares fitting and in most cases even three tilt angles would be sufficient. The differences between measured and mathematically predicted calibration curves were small, in the order of tens of nm, and can be regarded a characteristic of the stage, as similar results were obtained for a normal and an ultra-high-tilt sample holder.

One could envision several scenarios for the implementation of pre-calibration measurements. (A) For the best performance regarding accuracy (and the worst

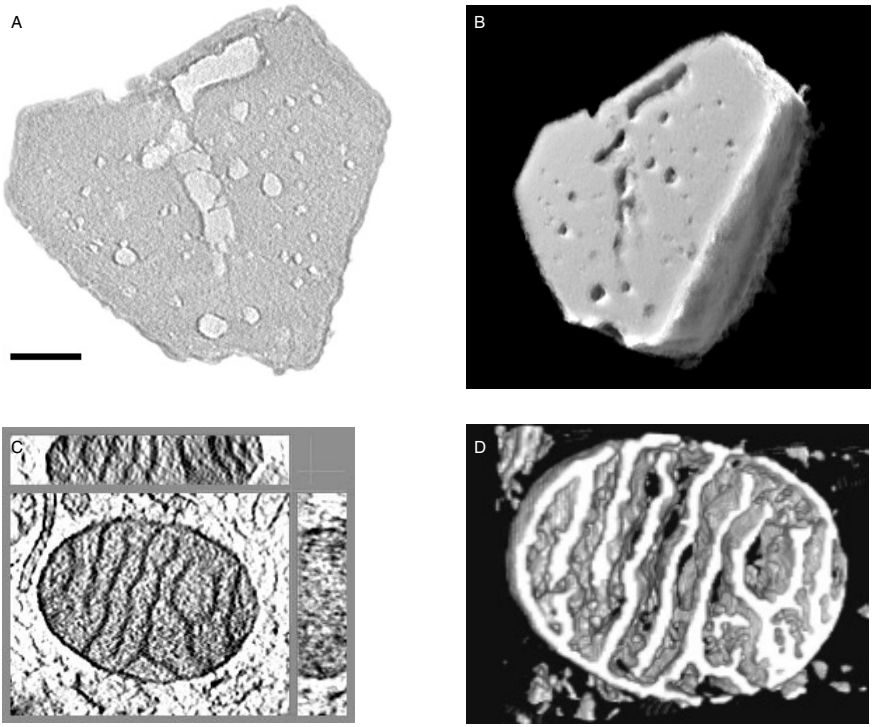

Fig. 7. Two reconstructions calculated from images acquired with pre-calibration electron tomography. (A) and (B) a zeolite crystal. (A) Slice through the volume, scale bar 100 nm. (B) Surface rendered view. (C) and (D) part of a mitochondrion in a semi-thick section (150 nm) of high-pressure frozen and freeze-substituted murine dentritic cells. (C) Slices through the volume (top *xz*-, bottom *xy*- and right *zy*-plane). (D) Surface rendered view.

regarding acquisition speed) the parameters of the rotational movement should be estimated from a few measurements (e.g. –30°, 0°, +30° at low magnification) and consequently be corrected for. Next, a full pre-calibration curve can be measured (e.g. with 5° increments at high magnification) to detect remaining image shifts of a few tens of nm with an accuracy of about 10 nm. Finally, during data acquisition (e.g. with 1° increment at high magnification), additional cross-correlation of images can ensure high accuracy in case of e.g. drift. (B) If relatively large image shifts during data acquisition do not occur because, e.g. the absence of drift, a single

pre-calibration measurement (e.g. with 5° increments at low magnification) together with a moderate number of drift corrections should be sufficient (and will take a few minutes less) to ensure proper data acquisition. (C) In a lot of cases at, e.g. moderate magnifications, the image feature of interest set close to eucentricity and the knowledge that the distance of the tilt to the optical axis is small, it will be possible to bypass the measurement of a pre-calibration curve and estimate (and adapt) the unknown parameters of the mathematical model while collecting a tilt series ('on the go', which would save some more minutes).

We implemented a first version of pre-calibration electron tomography as a JavaScript macro (available for download, see section E) in the Tecnai Image and Analysis software (TIA). In the current version of pre-calibration electron tomography software, we did not implement procedures suitable for cryo electron tomography applications. Nevertheless, the pre-calibration approach can be extended with steps, which (1) compensate for disturbing effects due to image drift (which often occur with a cryo holder) and (2) that ultra-low-dose data collection can be carried out by taking a different area on the sample for recording a tilt series from the area for measuring the pre-calibration curve.

High-throughput collection of tilt series could be combined with advanced automated relocation approaches (Potter et al., 1999; Pulokas et al., 1999; Carragher et al., 2000): (1) specific structures are identified on a microscope grid (manually or automatically) of which tilt series are to be required; (2) the specified structures on the grid are automatically relocated and centered by (*xy*-) stage-movements; (3) measurement and compensation of image shifts and defocus changes by pre-calibration; (4) from each structure a tilt series is collected.

Three main advantages of our novel method of data collection for automated electron tomography based upon pre-calibration of image shifts and defocus changes are:

1. Identification of the displacement of the tilt axis from the optical axis and thus the possibility for compensation of any image shifts and defocus changes that are caused by this misalignment. Remaining shifts due to intrinsic characteristics of stage/specimen-holders can also be pre-measured and pre-corrected, enabling high-throughput during data acquisition, which allows users to concentrate on

sample preparation, setting up the (biological) essay and the discussion of results. At the time of writing, the microscope hardware (i.e. the Tecnai PC) could acquire 151 images (with 1° increment) in less than 20 min. On the same hardware, data collection with the conventional approach takes more than 100 min.

2. The quality of a tilt series can be significantly enhanced, because the amount of required focus-change compensation during data acquisition can be minimized. The alignment of the optical axis to the tilt axis of the specimen stage can be achieved by invoking an amount of image shift (as deduced from the mathematical model describing the effect of specimen tilt). Less focus change during data collection will result in (1) less image rotation and (2) less magnification change. As a consequence, practical implementation of 'on-the-fly' automated data acquisition, alignment and 3D reconstruction procedures (which do not depend on the presence of fiducial markers in the images to correct for magnification changes and image rotation due to focus changes) has become within reach.

3. The uncoupling of microscope-control calibration from data acquisition opens the field for novel acquisition modes. One could, for instance, acquire a first tilt series with large tilt increments (for e.g. a first reconstruction at reduced resolution) and then include the images at intermediate tilt angles successively. The usage of acquisition modes other than bright-field and detectors other than a CCD camera or film becomes possible. For instance, taking tilt series in STEM mode, possibly in combination with EDX or electron energy loss spectroscopy to gain element specific information of the sample, could have important applications in biological and materials sciences. In biological sciences, ultrasmall gold labels tagged to the molecular structure of interest, e.g. embedded in thick (high-pressure frozen, freeze-substituted) stained and plastic-embedded sections (Starink et al., 1995; Humbel et al, 1998) could be imaged in 3D with high contrast and possibly be distinguished from metal-labels of a different element (nickel, silver). For materials sciences, 3D structural maps, which cannot be gained by TEM bright-field imaging because of diffraction contrast, becomes possible by high angular annular dark-field Z-contrast imaging (Midgley et al, 2001) and high-resolution 3D elemental mapping by EFTEM imaging (Weyland et al, 2001).

Acknowledgements

We like to thank Dr Max Otten and Dr Auke van Balen (FEI/Philips Electron Optics, Eindhoven, The Netherlands) for helpful discussions regarding image movement under tilted stage conditions, remote control of a Tecnai TEM and electron tomography in general. We are grateful to Dr Hans de Ruijter (Emispec Inc., Tempe, AZ) for helpful discussions and providing us with an initial version of OpenTomography. Furthermore we would like to acknowledge Professor Emeritus John Geus (Utrecht University, The Netherlands) for the recognition of the potential of electron tomography in materials sciences.

The research of A.J. Koster has been made possible by a fellowship of the Royal Netherlands Academy of Arts and Sciences (KNAW). The research of U. Ziese is supported by KNAW and the research of W.J.C. Geerts by FEI/Philips.

Addendum: Applications—Zeolites and Golgi complex

Zeolites

Electron tomography is not limited to the biological sciences. Any sample that can be prepared for transmission electron microscopy (TEM) and that satisfies the condition that the registered image contrast must be a projection of a physical characteristic of the sample can be investigated. As such, electron tomography is a useful tool to study the three-dimensional (3D) architecture and composition of inorganic solids (e.g. solid catalysts, photonic crystals and electronic devices), hundreds of nm in size at nm-scale resolution, complementing other techniques in the characterization of such materials (Koster et al., 2000).

Zeolites are key catalytic materials in applications such as hydro-isomerization of alkanes and hydrocracking of heavy petroleum fractions. One of the features of zeolites is the molecular dimension of their micropores, which are often advantageous to induce shape selectivity, but enhanced accessibility is frequently desirable to restrict mass transfer effects and/or allow catalytic conversion of larger molecules. Several approaches have been followed to enhance accessibility; i.e., the development of zeolites with intrinsically larger pores (Freyhardt et al., 1996), delaminated zeolite precursors (Corma et al., 1998), and the use of zeolite nanocrystals (Mintova et al., 1999). Besides accessibility, also the location of the catalytic active phase (e.g. metal particles) on the zeolite is important for the performance of the catalyst.

We have applied electron tomography to the study of several of these materials. For instance, we have shown that metal particles in zeolite crystals (Ag/NaY) can readily be located by electron tomography (Koster et al., 2000). As the location of the metal function inside or outside the micropores can strongly affect the selectivity of the catalyzed reaction, knowledge on the location of the metal function is crucial to steer catalyst synthesis (Maschmeyer et al., 1995; Creyghton et al., 1996). In another example we have visualized mesopores (see Figs. 7A and 7B; Koster et al., 2000; Janssen et al., 2001 and 2002) in zeolite crystals. It has been established that microporous zeolite crystals can be treated (acid leaching and/or steaming) to generate mesopores that greatly enhance accessibility and thereby catalytic activity

and stability (Alfredsson et al., 1993; Choi-Feng et al., 1993; Sasaki et al., 1995 and 1998; Meima, 1998).

Certain inorganic solids can be unsuitable to investigate by bright-field transmission electron tomography as they show angle dependent diffraction contrast due to their crystalline structure and thus do not adhere to the condition that the recorded image contrast must be a projection of their mass density according to the tilt angle. However, it has been shown that the problem can be overcome when these materials are investigated by high angular annular dark-field (HAADF) scanning transmission electron microscopy (STEM) instead of TEM tomography (Midgley et al., 2001).

Golgi complex

Cells are highly dynamical and extremely complex 3D objects. Understanding how cells function requires knowledge of cellular structures and organelles in time and space. A truly 3D analysis of cellular structures with a spatial resolution in the nm-range is only possible by electron tomography. The technique is particularly useful in the analysis of polymorphous organelles that may have sizes up to several hundred nm.

One of these organelles is the Golgi complex. In the classical vesicular transport model, the transport carriers are proposed to be small vesicles (50–100 nm in diameter) that bud from donor and fuse with acceptor organelles (Rothman and Wieland, 1996). Recently however, it has become apparent that also non-vesicular structures mediate membrane transport. For example, large supramolecular cargoes move through the Golgi complex without entering carrier vesicles (Bonfanti et al. 1998), and the endoplasmic reticulum (ER) to Golgi (Fig. 8; Geerts et. al, 2002) and Golgi to plasma membrane transport carriers are large (saccular) tubular structures instead of small vesicles (Polishchuk et al., 2000; Mironov et al., 2001). A unifying vesicular paradigm for transport carriers is therefore no longer sustainable and the structure and dynamics of the transport carriers that mediate intracellular membrane traffic need to be carefully re-examined using electron tomography.

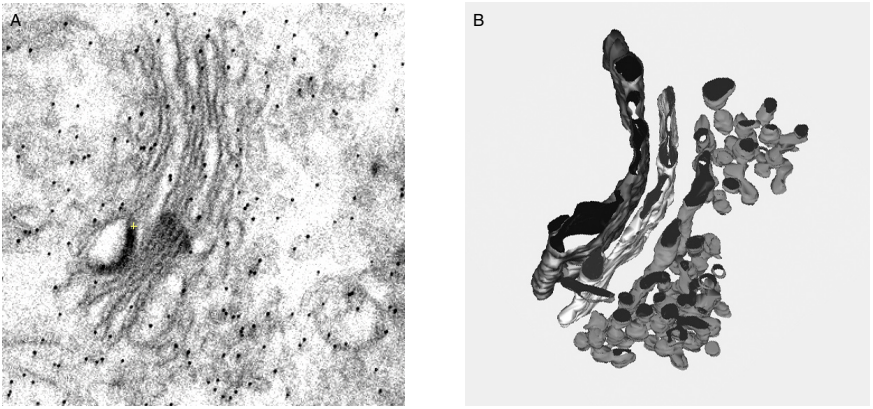

Fig. 8. (A) Electron micrograph of the Golgi complex in a 200 nm thick section of nocodazole treated normal rat kidney (NRK) cells. (B) Model gained by drawing the outlines of two cisternae (left) and the connections between the 'vesicles' (right) of the vesicular tubular cluster (VTC) of the 3D reconstruction of the Golgi complex shown in (A).

Chapter 3

Correction of autofocusing errors due to specimen tilt for automated electron tomography

ULRIKE ZIESE, WILLIE J.C. GEERTS, THEO P. VAN DER KRIFT, ARIE J. VERKLEIJ & ABRAHAM J. KOSTER

Abstract

Transmission electron microscopy images acquired under tilted-beam conditions experience an image shift as a function of defocus settings—a fact that is exploited as a method for defocus determination in most of the automated tomography data collection systems. While the method was shown to be highly accurate for a large variety of specimens, we point out that in its original design it can strictly only be applied to images of untilted samples. The application to tilted samples and thus in automated electron tomography is impaired mainly due to a defocus change across the images, resulting in reduced accuracy. In this communication we present a method which can be used to improve the accuracy of the basic autofocusing procedures that are currently used in systems for automated electron tomography.

Journal of Microscopy, accepted after revision.

Introduction

Electron tomography is a versatile method for obtaining three-dimensional (3D) information of biological and materials sciences samples (100–500 nm thick) with 2–20 nm resolution by transmission electron microscopy (TEM) (Frank, 1992). Electron tomography is generally applicable to isolated particles (e.g. macromolecules) as well as to pleomorphous structures like the Golgi complex or other cellular organelles, whole cells, or tissue sections. For recent reviews on electron tomography we refer to McEwen and Marko (2001) and to Baumeister et al. (1999).

The basic concept of electron tomography was outlined in the late sixties (Hart, 1968; DeRosier and Klug, 1968; Hoppe et al., 1968; Crowther et al., 1970) but a number of technical obstacles, concisely described in the mid-seventies (Hoppe et al., 1976; Hoppe and Hegerl, 1980), prevented realization of its potential until the mid-nineties. The basic procedure of electron tomography consists of two steps: data collection and data processing. For data collection, a series of two-dimensional (2D) projection images of a specimen tilted over a wide angular range is acquired (so called tilt series). Typically, a tilt series consists of 50–150 digital images (recorded with a CCD camera) taken over an angular range of –70° to +70°. After data collection a reconstruction step is carried out that comprises alignment of the projection images and 3D reconstruction typically via filtered back-projection. For a description of 3D electron microscopy, including electron tomography and some aspects of the data processing involved, we refer to Baumeister and Steven (2000).

In the mid-nineties, data collection systems became available (Dierksen et al., 1992; Koster et al., 1992; Dierksen et al., 1993; Grimm et al., 1997; Koster et al., 1997; Rath et al., 1997) that were capable of collecting a tilt series in an automated fashion. To collect a useful tilt series, two conflicting requirements needed to be reconciled. First, a tilt series has to be recorded that covers as wide an angular range as possible in as many increments as possible. Second, the electron dose has to be kept low to avoid radiation damage of the specimen. Due to the mechanical movement of the specimen when the stage is tilted, the focus and image position will change during collection of a tilt series. With the advent of computer controlled microscopes and large area digital cameras (CCD cameras), it became possible to implement automated

procedures for the repetitive (50–150 times) measurement and correction of (a) defocus (autofocus) and (b) image shifts (autotracking). Presently, automated data collection software packages, which correct for the movement of the specimen during data collection, are available both commercially and within the scientific community.

During the last five years we applied electron tomography in our laboratory as a tool for 3D structural investigations of both biological and materials sciences samples (e.g. plastic-embedded and stained sections, 100–300 nm thick; negatively stained isolated structures, 50–100 nm in diameter; frozen-hydrated viruses and tubular structures; zeolite particles, 50–200 nm).

In the course of time, we observed that the automatic focusing at higher tilt angles (> 50°) was often inaccurate. The variability in focusing accuracy became more apparent after developing the pre-calibration data collection approach (Ziese et al., 2002), where the image shifts and focus changes are measured (calibrated) as a function of specimen tilt prior to data collection. Though the focus generally changed smoothly with specimen tilt, as expected, occasionally large focus changes were measured at the higher tilt angles. These errors could be several μm in magnitude, which is sufficiently large to seriously limit the resolution and reliable interpretation of a tilt series.

In this communication we propose a significant modification of the autofocus method as it is currently implemented in practically all of the available automated data collection systems. The modified method is designed to work on highly tilted specimens and is suitable for automatic focusing as part of an automated procedure to collect tilt series. At the higher tilt angles the modified method performs more reliably than without a correction for specimen tilt.

Beam-tilt autofocus method

With the tilted-beam method two images are taken, each acquired with a different beam tilt. Fig. 1 shows a schematic diagram of the projection of an untilted specimen, with a certain defocus D_0 and beam tilt $\vec{b}$. In comparison to an image taken without beam tilt, the image will be shifted by

$$\vec{s} = D_0 * \tan(\vec{b}) \quad (1)$$

For a known beam tilt it is therefore possible to determine the defocus by measuring the image shift that is given by the cross-correlation of two images acquired with different beam tilts. For the sake of clarity, the effects of astigmatism, misalignment, as well as beam-tilt induced defocus, are not taken into account in equation (1).

Though the beam-tilt method has shown to be highly accurate for untilted specimen (5–50 nm; Dierksen et al., 1993), the method can be far less accurate for tilted specimens. Fig. 2 shows the projection images of a Epon-embedded section of a bullfrog saccular hair cell at tilt angles of –70°, 0° and 0°. While the whole area of 3.2 μm × 3.2 μm of the image displays the same defocus at 0°, it can be seen that the defocus varies across the image at –70° (right side blurry) and +70° (left side blurry). The defocus difference between the edge and the center of the image is 4.4 μm (3.2 μm/2 × tan (70°)) for the tilted views.

Defocus determination by the beam-tilt method for tilted samples is thus impaired by an elongation of the cross-correlation peak, which has contributions from areas with different defocus values. In an unfavorable case, the autofocus procedure could focus on a high-contrast region near the edge of the field of view and, consequently, measure a defocus value several μm different from the defocus present in the center of the image. At lower magnifications the field of view of the CCD camera will be relatively large—resulting in a large error in defocus measurement. The problem should therefore especially be kept in mind if the defocus is determined at a lower magnification than that used for image acquisition as e.g. possible with pre-calibration electron tomography (Ziese et al., 2002) or with large area (2k × 2k and 4k × 4k pixel) CCD cameras.

Fig. 1. Schematic diagram of defocus D_0 and beam tilt $\vec{b}$ induced image shift $\vec{s}$ of the projection of an untilted specimen.

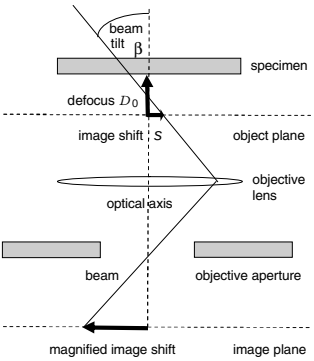

Fig. 2. Projection images of an Epon-embedded section of a bullfrog saccular hair cell at tilt angles of –70° (left), 0° (middle, 3.2 µm × 3.2 µm) and +70° (right). The defocus was about –10 µm in the center of the images but varies across the tilted images by 8.8 µm (images are partly blurred).

In this communication we examine the location of image features under tilted-sample, tilted-beam conditions and present a method that improves the defocus measurement under these conditions.

Modification of the beam-tilt method for tilted specimen

Fig. 3(left) shows the general geometry of a beam-tilt induced image shift $\vec{s}$ in the image *xy*-plane. The angle between the sample-tilt axis and the image *y*-axis is γ and the angle between the image shift $\vec{s}$ as induced by the beam tilt and the tilt axis is δ. For the further discussion, however, we assume that the sample-tilt axis goes through the center of the image and is parallel to the image *y*-axis ($\gamma = 0°$). The image is assumed to be in focus along the tilt axis and the image shift $\vec{s}$ assumed to be parallel to the *x*-axis ($\delta = 90°$, $s_y = 0$, $\vec{s} = s_x$ Fig. 3(right)). Fig. 4 displays the location of image features of a tilted sample without and with beam tilt b. The upper row shows the positions in the *xz*-, the middle row in the *xy*-plane.

When a tilted sample is imaged, the defocus *D* of an image feature depends on the *x*-coordinate and the sample-tilt angle a.

$$D = x * \tan(a) \tag{2}$$

From (1) and (2) it follows that the image shift $\vec{s}$ of such a feature will be

$$\vec{s} = x * \tan(a) * \tan(\vec{b}) \tag{3}$$

Thus, the further the feature is away from the center of the image—and thus away from the focus plane—the larger the image shift will be. Furthermore, the image shift will be positive for positive defocus and negative for negative defocus, when the beam tilt is in one direction and the reverse for a beam tilt in the opposite direction. The bottom row of Fig. 4 shows the image shifts that will be indicated by the cross-correlation of different areas of the beam-tilted and not beam-tilted images of the sample, displayed as vector fields.

Therefore, to ensure that all areas of the images give rise to the same cross-correlation peak, it is necessary to squeeze/stretch the $\pm b$ beam tilted images parallel to the *x*-axis and with respect to the *y*- (sample-tilt) axis:

$$stretch(a, \pm b) = 1 + \tan(a) * \tan(\pm b) \tag{4}$$

If the beam-tilt angle is not known, it can be calibrated from the image shift measurement of an untilted sample for a known defocus using (1).

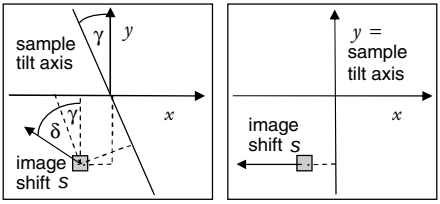

Fig. 3. General geometry of beam tilt induced image shift in the image xy–plane (left). The angle between the sample-tilt axis and the image y-axis is γ and the angle between the image shift $\vec{s}$ and the tilt axis is δ. The right side shows the special case when the sample-tilt axis is parallel to the y-axis and the image shift is parallel to the x-axis as discussed in this publication.

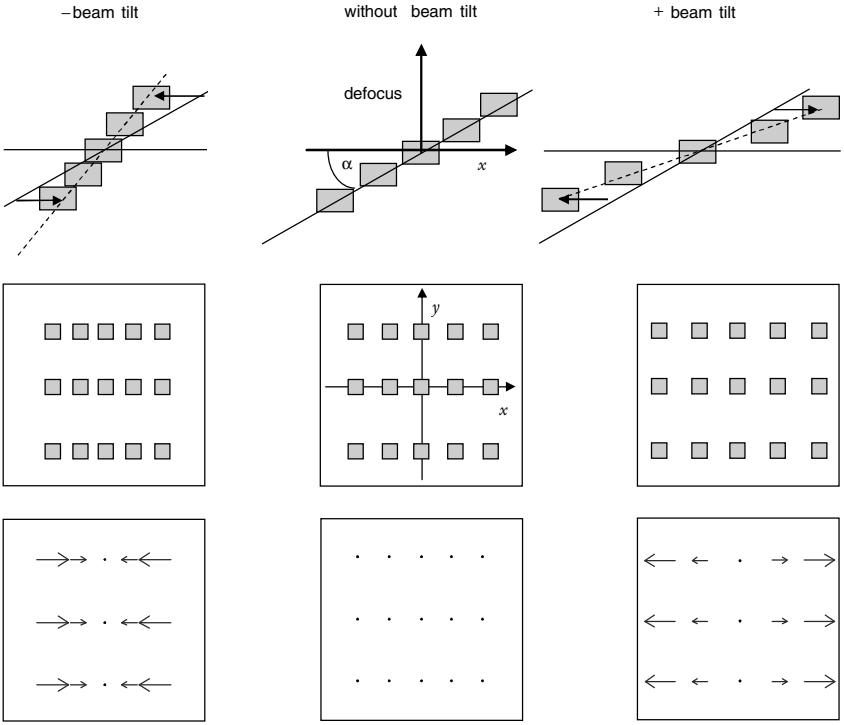

Fig. 4. Location of image features of a tilted sample without and with beam tilt b. The upper row shows the positions in the xz-, the middle row in the xy-plane. The bottom row shows the image shifts that will be indicated by the cross-correlation of different areas of the beam-tilted and not beam-tilted images of the sample, displayed as vector fields.

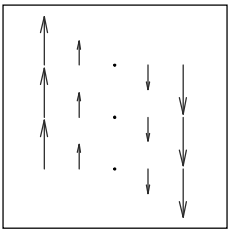

Fig. 5. Image shift vectors of a tilted sample for the special case when both sample-tilt axis and image shifts are parallel to the image *y*-axis. The image appears 'sheared'.

From (4) the relative stretch between the $+b$ and $-b$ beam-tilted images can be calculated.

$$rel.stretch = \frac{stretch(a+b)}{stretch(a-b)} = \frac{1+\tan(a)*\tan(b)}{1-\tan(a)*\tan(b)} = \frac{\cos(a-b)}{\cos(a+b)} \qquad (5)$$

Note that this equation is the same as the cosine stretch for the cross-correlation of two images acquired at $(a-b)$ and $(a+b)$ sample-tilt angles (Guckenberger et al., 1982). It can be interpreted in the way that an image acquired under a certain sample-tilt angle a and beam-tilt angle b is the same as one acquired under a sample-tilt angle $(a-b)$.

In the general case, when neither the sample-tilt axis is parallel to the *y*-axis nor the beam-tilt induced image shift is in a direction perpendicular to the *y*-axis ($\gamma \neq 0°$ and $\delta \neq 90°$ and $\delta \neq 270°$), the image transformation can be determined by substituting *x* in equation (3) with the distance between the sample feature and the sample-tilt axis. Fig. 5 depicts the special case when $\gamma = 0°$ and $\delta = 0°$, which is equivalent to an image shear.

Experimental verification

To evaluate the improvement in defocus determination of tilted samples by the beam-tilt method after application of the presented formulas, we acquired a series of images on a 200-kV Tecnai 20 transmission electron microscope (FEI Co., Eindhoven, The Netherlands) with a bottom-mounted slow-scan CCD camera (TemCam F214, Tietz Video and Image Processing Systems GmbH, Gauting, Germany). The camera is composed of 2048 × 2048 square pixels of 14 μm. At a nominal magnification of 5000× (post-magnification of 1.8×, binning 2) the calibrated pixel size was 3.1 nm and the images represented a specimen area of 3.2 μm × 3.2 μm. Image acquisition was performed under remote control by a JavaScript macro, which communicated with the microscope via the TIA and Tecnai Scripting software (FEI Co.).

We used beam-tilt values of $T_x = 0.02000$ and $T_y = 0.02038$ (the '+' beam tilt), and $T_x = -0.0200$ and $T_y = -0.02038$ (the '–' beam tilt). The named values are in arbitrary units (as indicated by the Tecnai Scripting software) and gave rise to image shifts almost parallel to the *x*-axis of the CCD images. The shifts were therefore also almost perpendicular to the sample-tilt axis that was nearly parallel to the CCD image *y*-axis (about 6° off). We acquired images for '+' beam-tilt and '–' beam-tilt illumination conditions for sample-tilt angles α of –56°, –40°, –20°, 0°, +20°, +40°, and +56°.

Image processing was performed with MATLAB (The MathWorks, Inc., Natick, MA) on a PC running under Windows XP (Microsoft Co., Redmond, WA).

Results and Discussion

We extracted 9 small areas of a size of 128 × 128 pixels from the 1024 × 1024 pixel images, which we had taken for '+' and '–' beam-tilt illumination conditions and for each tilt angle (Fig. 6).

Fig. 7 displays the image shifts and cross-correlation functions (XCFs) for the sample-tilt angles of –56°, –40°, +40°, and +56° (from left to right). The 1st row shows the image shifts between the corresponding areas for '+' and '–' beam-tilt images, which are calculated via cross-correlation and displayed as vector fields. All image-shift vectors for all tilt angles are perpendicular to the image *y*-axis and their size and orientation depends on the *x*-coordinate inside the images. Comparison with the displacement maps of Fig. 4 shows that this is exactly what was expected (when the center of the images was not in focus). Following equation (5)—and with a beam tilt of 5 mrad—the image shifts could be made the same throughout the images when one of the beam-tilted images was stretched in the *x*-direction before cross-correlation. The 3rd row of Fig. 7 shows the displacement fields after correction. The 4th row shows the central part of the XCF that was calculated from the full images. The broadening of the cross-correlation peak is less severe than in the uncorrected case (2nd row of Fig. 7).

Fig. 8 compares the contributions of different types of errors in defocus determination for different magnifications at a sample-tilt angle of 60°. The theoretical comparison assumes an experimental set-up with a CCD camera with 2048 × 2048 pixels with a size of 14 μm, a post-magnification of 1.8× and a beam tilt of 4 mrad. The figure includes values for the calculated errors caused by (a) a broadening of the peak due to a sample thickness of 100 nm, which is the same for all magnifications, (b) a limited accuracy in the measurement of the location of the XCF peak of 1 pixel and the use of (c) only the central 25% or (d) an additional 75% (and thus 100%) of the beam-tilted images for cross-correlation. The use of only a central part of the images is routinely done in programs for the automated acquisition of electron tomography tilt series to improve defocus determination. However, in spite of these attempts, the errors can still be as large as several μm at high tilt angles and low magnifications, when no correction for specimen tilt is taken into account.

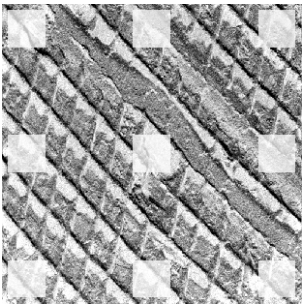

Fig. 6. One of the 1024 × 1024 pixel (3.2 µm × 3.2 µm) images of a calibration grid that were used to evaluate the improvement in defocus determination of tilted samples by the method presented in this publication. The overlay indicates the 128 × 128 pixel sized areas from which the shifts between the '+' and '–' beam-tilt images were calculated.

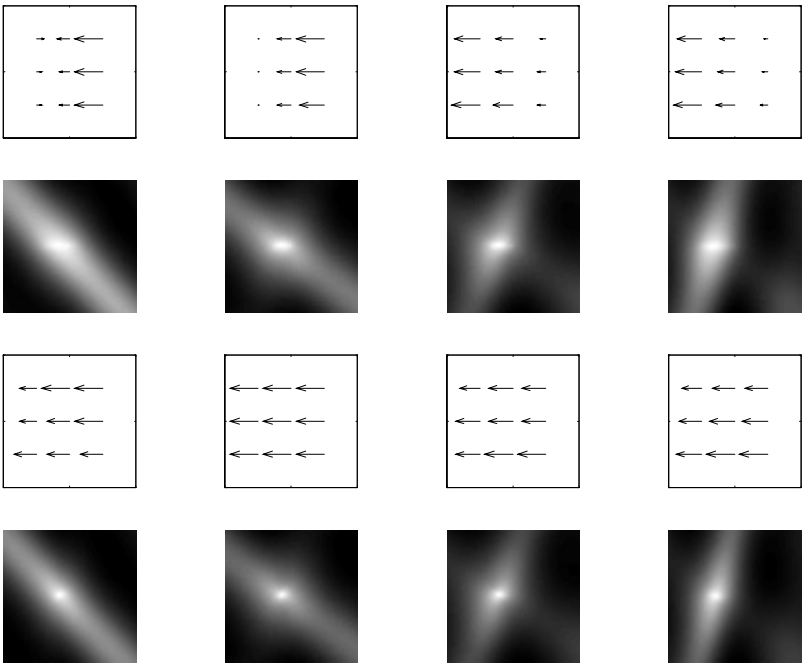

Fig. 7. Image shifts between corresponding areas (see Fig. 6) for '+' and '–' beam-tilt images for sample-tilt angles of –56°, –40°, +40° and +56° (from left to right) without (1st row) and with (3rd row) correction for sample tilt. The 2nd and 4th rows show the central part of the cross-correlations that were calculated from the full images of the uncorrected and corrected images. The broadening of the cross-correlation peak is less severe in the corrected case.

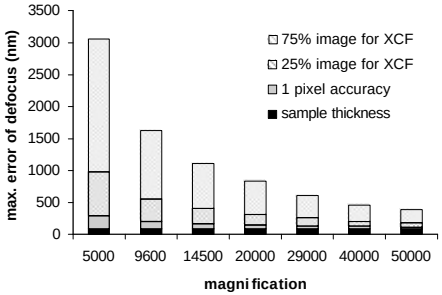

Fig. 8. Comparison of the contributions of different types of errors in defocus determination for a sample-tilt angle of 60° and a beam tilt of 4 mrad at different magnifications (see text for details).

The possible errors in defocus determination from (c) and (d) due to the defocus ramp within the two images acquired for automatic focusing will—theoretically—be completely avoided by stretching the two images by an amount given by relations (4) or (5). Therefore, we strongly recommend that stretching be incorporated into existing data collection systems as it is an essential modification for accurate beam-tilt based autofocusing methods. The practical achievable accuracy in the presented correction depends on the accuracy to which the sample-tilt angle (due to a possible—but unknown—pre-tilt of the sample) and the beam-tilt angle (due to misalignment or reproducibility in the direction of the beam) are known. If we assume for instance that the sample-tilt angle is known to an accuracy of 10° than the suggested correction will only be beneficial for sample-tilt angles greater than that value.

Conclusions

We have modified the defocus measurement method based upon beam-tilt induced image shifts to be suitable for automated electron tomography. This is necessary because defocus variations across the sample significantly degrade the accuracy of current beam-tilt autofocus methods—giving unreliable measurements. We have shown that the problem can be overcome by stretching the beam-tilted images prior to cross-correlation by a factor that can be derived from four parameters of the data collection set-up: (a) the orientation of the sample-tilt axis, (b) the sample-tilt angle α, (c) the orientation (direction) of the beam-tilt axis, and (d) the beam-tilt angle β. In the case that the sample-tilt axis is parallel to the image *y*-axis and the beam-tilt induced image shift is parallel to the *x*-axis, the required stretch would be

$$stretch(\alpha, \pm\beta) = 1 + \tan(\alpha) * \tan(\pm\beta).$$

We emphasize that even if the problem might not be directly visible to the human eye by looking at the original images (the stretch is e.g. just 1.007 for $\alpha = 60°$ and $\beta = 4$ mrad), it can lead to relatively large errors in defocus determination (several μm). We suggest that the correcting stretch should be routinely applied when using the beam-tilt method to determine the defocus for automated electron tomography.

Acknowledgements

We would like to thank Manfred Auer (Skirball Institute of Biomolecular Medicine, NYU and The Rockefeller University) and Jim Hudspeth (HHMI and The Rockefeller University) for sections of bullfrog saccular hair cell stereocilia and David Agard (Macromolecular Structure Group, UCSF) for critical reading of the manuscript.

The research of U. Ziese and A.J. Koster (fellowship) has been made possible by support of the Royal Netherlands Academy of Arts and Sciences (KNAW).

Chapter 4

Three-dimensional localization of ultrasmall immuno-gold labels by HAADF-STEM tomography

ULRIKE ZIESE, CHRISTIAN KÜBEL, ARIE J. VERKLEIJ & ABRAHAM J. KOSTER

Abstract

The localization of scarce antigens in thin sections of biological material can be accomplished by pre-embedment labeling with ultrasmall immuno-gold labels. Moreover, with this method, labeling is not restricted to the section surface but occurs throughout the section volume. Thus, when combined with electron tomography, antigens can be localized in three dimensions in relation to the three-dimensional (3D) ultrastructure of the cell. However, for visualization in a transmission electron microscope, these labels need to be enlarged by silver or gold enhancement. The increase in particle size reduces the resolution of the antigen detection and the large particles obscure ultrastructural details in the tomogram. In this paper we show for the first time that these problems can be avoided and that ultrasmall gold labels can be localized in three dimensions without the need for gold or silver enhancement by using high angular annular dark-field scanning transmission electron microscopy (HAADF-STEM) tomography. This method allowed us to three-dimensionally localize Aurion ultrasmall goat anti-rabbit immuno-gold labels on sections of Epon-embedded, osmium-uranium-lead-stained biological material. Calculations show that a 3D reconstruction obtained from HAADF-STEM projection images can be spatially aligned to one obtained from transmission electron microscopy (TEM) projections with subpixel accuracy. We conclude that it is possible to combine the high-fidelity structural information of TEM tomograms with the ultrasmall label localization ability of HAADF-STEM tomograms.

Journal of Structural Biology 138 (© 2002) 58–62, Elsevier Science (USA).

1. Introduction

Postembedment immuno-gold labeling has been shown to be very successful in localizing molecules in thin sections of biological material. If the structure under study is unaffected by the preparation, cryo-ultramicrotomy after mild chemical fixation according to Tokuyasu (1973) is the preferred method. An alternative method is freeze substitution of specimens frozen by high-pressure freezing, which is in principle a better method for structural preservation, in combination with immunolabeling (for a review see Verkleij et al., 1999). As long as one keeps in mind that structural damage due to permeabilization of the cells might be a problem, preembedment labeling, where antigens can be reached throughout the specimen, can be regarded as the only method for the detection and visualization of scarce antigens and three-dimensional (3D) studies at the electron microscopic level (Humbel et al., 1998). Usage of the small antibody fragment Fab in combination with ultrasmall gold particles has been shown to be successful (reviewed in Hainfeld et al., 1999). As these ultrasmall gold particles are not visible in transmission electron microscopy (TEM) images of thin sections, they are subsequently enlarged by silver (Danscher, 1981) or gold (Hainfeld and Powell, 2000) enhancement. By TEM stereomicroscopy (Starink et al., 1995) the labeled antigens can be visualized in three dimensions.

As it is known that ultrasmall labels can be detected without silver enhancement in two-dimensional high angular annular dark-field scanning transmission electron microscopy (HAADF-STEM) imaging (Hainfeld et al., 1999; Stierhoff et al., 1992), we have extended HAADF-STEM imaging to three dimensions via HAADF-STEM tomography. Successful experiments using STEM tomography of biological sections have been carried out previously (Beorchia et al., 1993) and recent experiments on HAADF-STEM tomography indicate that resolutions of at least 1 nm can be obtained for material science samples (Midgley et al., 2001; and own experiments).

As a first step in the study, we have applied ultrasmall colloidal gold labels to the surface of conventionally prepared, Epon-embedded, osmium-uranium-lead-stained sections of bullfrog saccular hair cell stereocilia. It was thus possible to investigate the detectability of ultrasmall labels without the need of silver enhancement in the

presence of heavy metal stain by the proposed method of HAADF-STEM tomography.

As the HAADF-STEM signal is approximately proportional to the square of the atomic number, the method is suited to detect small clusters of material with a higher density than the surrounding area. However, for the imaging conditions chosen, the HAADF-STEM reconstruction of the stained bullfrog stereocilia did not exhibit the same details for the biological features as a tomogram obtained from a TEM tilt series. We have therefore spatially aligned the 3D reconstruction calculated from HAADF-STEM projection images with one that was obtained from TEM projections of the same sample area, combining the advantages of both imaging modes.

2. Materials and methods

Sections of bullfrog saccular hair cells were provided by Manfred Auer and A. James Hudspeth as part of an ongoing collaboration on the structure of the mechano-electrical transduction and adaptation machinery in stereocilia and were obtained by conventional processing of epithelial tissue including chemical fixation, a progressive lowering of temperature dehydration scheme, followed by Epon embedding. The sample was exposed to stains containing osmium, uranium, and lead. Before TEM data acquisition 10-nm and after TEM and before STEM data acquisition 6-nm and ultrasmall (average particle size 0.8 nm) goat anti-rabbit immuno-gold labels (Aurion, Wageningen, The Netherlands) were absorbed to the sections for 30 min.

At first, the sample was mounted in a Gatan Model 670 ultra-high-tilt holder and a TEM tilt series was acquired on a 200-kV Tecnai 20 (S) transmission electron microscope (FEI Co., Eindhoven, The Netherlands) from −75° to +72° (1° increment). Images were recorded with a bottom-mounted slow-scan CCD camera (TemCam F214, Tietz Video and Image Processing Systems GmbH, Gauting, Germany) that is composed of 2048 × 2048 square pixels of 14 μm. At a nominal magnification of 19000×, the calibrated pixel size was 0.82 nm. The images represented a specimen area of 840 nm × 840 nm. For the image

acquisition we made use of automated data collection procedures implemented as JavaScript macros (Ziese et al., 2002) in the TIA software (Tecnai Imaging and Analysis).

Next, STEM experiments were performed on a 200-kV Tecnai F20 SuperTwin transmission electron microscope (FEI Co.) with the sample mounted in a modified FEI single-tilt holder. We used an extraction voltage of 3.85 kV, gun lens 7, spot 10, and a 70-μm C2 condenser aperture. These settings correspond to a spot size of approximately 0.3 nm and a current density of 0.6 pA/Å^2. Fourty-seven projections were recorded with an on-axis HAADF detector for tilt angles from –54° to +38° (2° increment, the tilt range was limited due to the geometry of the holder, which shaded the specimen at higher tilt angles.). With a dwell time of 10 μs/pixel (40 sec/image), the electron dose corresponded to 70 e^-/Å^2 for each tilt increment. The camera length was 100 mm to ensure detection of incoherently scattered electrons only. The nominal magnification was 110000× and the scanned image represented a specimen area of 934 × 934 nm^2 (2048 × 2048 pixels of 0.46 nm). Images were acquired via the TIA software with manual focusing and alignment.

Image processing was performed on a UNIX workstation (Octane2 dual-processor 2 × 400 MHz R12000, Silicon Graphics Inc., Mountain View, CA) with IMOD (Kremer et al., 1996) and IVE (Fung et al., 1996) and on a PC running under Windows 2000 (Microsoft Co., Redmond, WA) with Amira (TGS, Merignac, France) and MATLAB (The MathWorks, Inc., Natick, MA). IMOD was used to calculate 3D reconstructions of the TEM and STEM projections and afterward for fitting the STEM to the TEM tomogram. Amira was used for visualization, IVE was used for extracting line scans through the reconstruction, and MATLAB was used for evaluating them. For reconstruction of the TEM tomogram, we made use of only the projections that were acquired under the tilt angles (–54° to +38°, 2° increment) that were also used in STEM mode. The section thickness as calculated from the reconstruction was 60 nm. The STEM projection images were binned to the same number of pixels (1024 × 1024) as the TEM images.

3. Results

Figs. 1a and 1b show the 0° TEM and STEM projection images of the same area of an Epon-embedded section of bullfrog saccular hair cell stereocilia. Stereocilia are investigated to gain insights into the mechano-electrical transduction pathway in hearing (reviewed in Hudspeth, 1997). They are cylindrical, actin-filled rods forming a hexagonal array, protruding from the apical cellular surface of hair cells. The upper part of the images shows part of the tallest stereocilium, and the lower part shows part of the kinociliar bulb. The stereocilium and kinociliar bulb are connected via thin extracellular filaments.

Fig. 1c visualizes the 3D reconstruction of the same area as shown in Figs. 1a and 1b, calculated from the HAADF-STEM projection images; 10-nm, 6-nm and ultrasmall immuno-gold labels are absorbed to the upper and lower surfaces of the section. The 3D location of all labels can be seen when viewed with red and green stereo glasses (see original publication for color figure). To facilitate the visibility of the labels in Fig. 1c we applied a 3 × 3 × 3 pixel Gaussian filter to the 3D reconstruction and processed it so that the image contains only a small percentage of volume-rendered material, overlaid with three transparent slices of the top, middle and bottom of the reconstruction. Some of the ultrasmall labels are highlighted by arrowheads.

Fig. 1d shows a 100-pixel-wide line scan within the tomogram through one of the ultrasmall labels. The average ratio for label signal to noise (mean maximum peak height rising above the mean of the surrounding area divided by mean standard deviation of surrounding area) over 15 of these labels was 5.5. A reconstruction calculated from every second projection (4° increment) gave a signal to noise ratio of 4.5. However, labels could not be detected visually when calculated from an even smaller number of projections. To determine whether the ultrasmall gold labels could be detected within a stained area, we took a 100-pixel-wide line scan through the heavily stained upper edge of the kinociliar bulb (Fig. 1e). Ultrasmall gold labels will be detected in stained areas when the stain signal is weaker than the ultrasmall gold signal. In our reconstruction the ratio for gold signal to stain signal was 4.0 on average, indicating that an ultrasmall gold label would be detectable when surrounded by heavy metal stain.

It was shown that the STEM tomogram can be aligned/registered to the TEM tomogram (data not shown) with subpixel accuracy. For alignment we used the part of IMOD that is generally used to merge the two parts of a double-tilt axis reconstruction. Alignment yields the affine transformation, containing the stretch, rotation, and shift necessary to register one volume with the other and is performed in two steps. An initial alignment is achieved by selecting a series of corresponding markers in the two reconstructions. The registration is then refined by the correlation of small volumes of the two reconstructions. Calculations indicated that the mean displacement of all analyzed volumes was 0.3 nm after alignment.

4. Discussion

We conclude that the small structures that were revealed by 3D reconstruction from HAADF-STEM projection images represent the ultrasmall immuno-gold labels that were absorbed to the sections, because (1) they are present at their expected location at the surfaces of the section, (2) their mass density is significantly higher than other parts of the reconstruction, and (3) the intensity in HAADF-STEM projection images is proportional to the square of the atomic number. Our findings are in agreement with recent work showing that structures of that size can indeed be visualized via HAADF-STEM tomography (Midgley et al. 2001; and own experiments).

Based on our experience with TEM tomography, the clear visibility of such small structures (Aurion reports an average size of 0.8 nm for these ultrasmall immuno-gold labels) in the STEM tomograms was quite unexpected for the following reasons: (1) the pixel size of 0.92 nm of the reconstruction and (2) the predicted resolution for a limited angle, single-axis tilt reconstruction of an extended slab (Radermacher, 1992) is sample thickness × increment(°) × π/180°/cos(maximum tilt angle) and thus about 3 nm for the specimen and imaging conditions chosen in our experiments. Regarding (1), we argue that the signal generated by a single ultrasmall immuno-gold label surrounded by less dense material (Epon, stain) is sufficiently strong to be visualized, even if the pixel size is binned to a value that is larger than the particle.

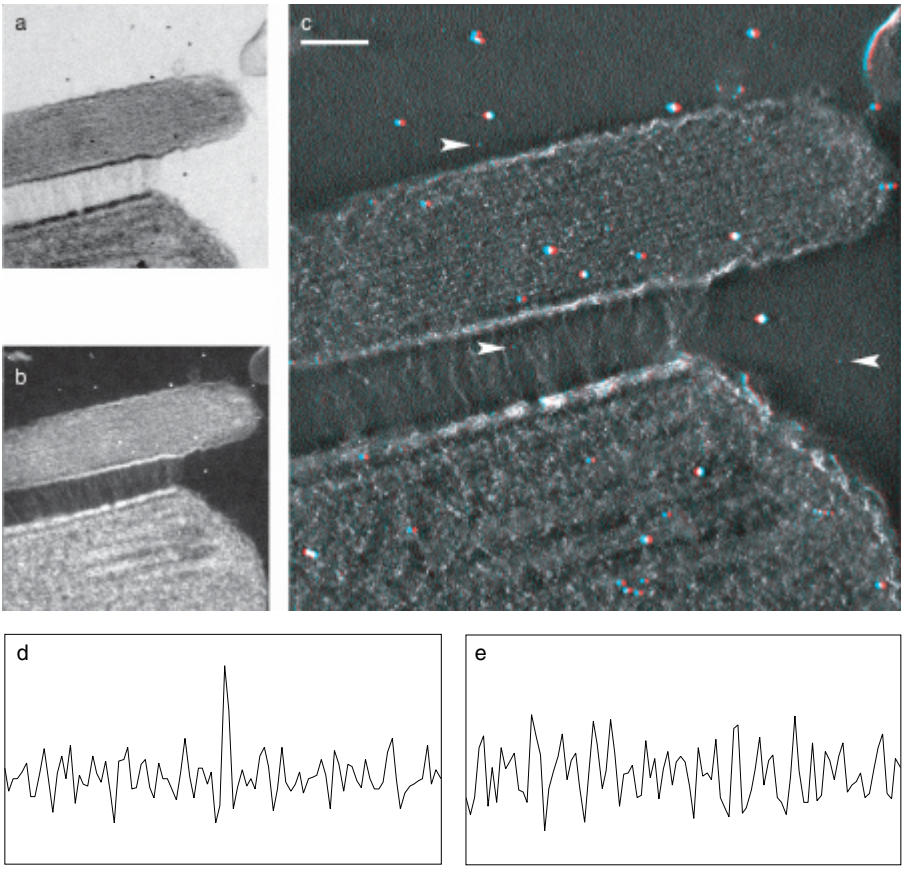

Fig. 1. (a) and (b) 0° TEM and STEM projection images of the same area of a section of bullfrog saccular hair cell stereocilia. (c) Red and green stereoview of the 3D reconstruction calculated from the HAADF-STEM projection images (scale bar 100 nm, see original publication for color figure). The image contains a small percentage of volume-rendered material, overlaid with three transparent slices of the top, middle, and bottom of the reconstruction. Arrowheads indicate some of the ultrasmall immuno-gold labels that are absorbed to the upper and lower surfaces of the section. (d) and (e) 100-pixel-wide line scans through the HAADF-STEM reconstruction of one of the ultrasmall labels and part of the upper edge of the kinociliar bulb. The y-axes are given in arbitrary units (scaling due to 3D reconstruction) and are the same for (d) and (e).

Furthermore, this intensity will probably even be sufficiently high to be detected when spread over several pixels when the scanning probe is not perfectly focused. Regarding (2), there are indications that the resolution of tomograms gained from HAADF-STEM projections is better than that given by the Radermacher formula. Midgley (personal communication) assumes a value of resolution = sample thickness/ 100 for a single-axis tilt series (our data were not taken under imaging conditions that allow verification of this assumption). One could further argue that the Epon resin is almost invisible to the beam compared to the gold labels and the stain. As such the 'sample thickness', as used in the Radermacher formula, would be a function of the amount of locally stained material, which would count in favor of the achievable resolution.

The potential of STEM tomography for application in structural and cell biology is high when we realize that even under the moderate imaging conditions used, ultra-small immuno-gold labels could directly be detected on Epon-embedded sections. Beam-broadening was no problem for the detection of labels on the bottom of the section for the 60-nm-thick section used (and as confirmed by a control experiment, data not shown) and should also not be the limiting factor for thicker samples, as a value of just 1 nm is predicted for a 200-nm-thick sample at 100 kV (Reimer, 1997). Finally, as labels were detected that were located over areas that were osmium-uranium-lead-stained, we conclude that HAADF-STEM tomography can be used for three-dimensional localization of ultrasmall immuno-gold labels—without the need of silver enhancement—even in the presence of heavy metal stain.

For the further investigation of the proposed method for the 3D localization of ultra-small immuno-gold labels by HAADF-STEM tomography, a number of quantitative assessments are required: for instance, experimental characterization up to what section thickness labels can be detected inside or on the top and bottom of the sections, and also, characterization of what amount of metal stain would be needed to align STEM and TEM tomograms successfully and up to what amount of surrounding metal stain ultrasmall immuno-gold labels can be detected, because strictly speaking we did not show that they are detectable *within* heavily stained portions of the section. Furthermore, a comparison is needed of the detectability of different immuno-labels, e.g. ultrasmall colloidal gold (8 Å, 15 Au atoms) from

Aurion (Wageningen, The Netherlands) and Nanogold (1.4 nm, 67 Au atoms) from Nanoprobes Inc. (Stony Brook, NY). Detection efficiency could be determined by immuno-labeling of periodic structures, such as actins. Finally, the optimum imaging conditions including the minimum dose and the minimal number of projection images needed for the detection of the labels must be determined. All four suggestions should be seen in the light that one ultrasmall gold particle made of 15 Au atoms yields the same signal as 2600 C, 16 Os, 14 Pb, or 11 U atoms. Finally, for the routine application of HAADF-STEM tomography, auto-tuning of STEM imaging (Baba et al., 2001) and automation of STEM tilt series acquisition (as suggested by Weyland, personal communication; Ziese et al., 2002) and in a similar fashion as done previously for TEM tomography, would guarantee optimal focusing (Koster et al., 1987), minimal electron dose (Koster et al., 1989), and fast acquisition times (Koster et al., 1992 and Ziese et al., 2002).

Acknowledgements

We thank Manfred Auer (Skirball Institute of Biomolecular Medicine, NYU and The Rockefeller University) and Jim Hudspeth (HHMI and The Rockefeller University) for sections of bullfrog saccular hair cell stereocilia, Matthew Weyland and Paul Midgley (Cambridge University, UK) for information on HAADF-STEM tomography, David Mastronarde (University of Colorado at Boulder) for explanations and modifications of the IMOD software, and Koert Burger (Utrecht University, The Netherlands) for critically reading the manuscript.

The research of U. Ziese and A.J. Koster (fellowship) has been made possible by support from the Royal Netherlands Academy of Arts and Sciences (KNAW).

Chapter 5

General discussion

Electron tomography is a powerful method with great potential for the three-dimensional (3D) characterization of samples in the nm-resolution range in the biological and materials sciences (Baumeister et al., 1999; Koster et al., 2000; McEwen and Marko 2001). It is unique for its ability to investigate individual structures, which sets it apart from 3D methods like angular reconstitution (electron microscopy), nuclear magnetic resonance spectroscopy (NMR), electron and X-ray crystallography that rely on averaging over unit cells or particles or the assumption of certain symmetries.

The general applicability pairs with a high demand on the versatility of the instrumentation, which typically includes a slow-scan CCD camera and a high-tilt sample stage and holders—apart from the need for a remote controllable electron microscope and, in addition, for the expertise necessary to operate this instrumental set-up. This led to a situation where electron tomography is mainly applied by, or in collaboration with, laboratories that are also involved in the software development for the automation/reconstruction of tomographic tilt series.

Recently this picture has begun to change. International congresses (Ringberg Castle, Germany, 1997; Amsterdam, The Netherlands, 2001), special issues of the *Journal of Structural Biology* dedicated to electron tomography, and various excellent applications that emerged in the last few years (see e.g. special issue of *JSB*, 138, 2002) illustrated the power of electron tomography and a wider audience has become interested in the routine inclusion of the method in their investigations.

Manufacturers of electron microscopes (FEI Co., Eindhoven, The Netherlands; JEOL, Ltd., Akishima, Japan) as well as independent suppliers of hard-/software for electron microscopy (Emispec, Inc., Tempe, AZ; TVIPS, GmbH, Gauting, Germany), have seen the signs on the wall and provide systems for the automated collection of tilt series that include not only the latest developments that evolved in the specialized laboratories, but can also be used by non-experts. Members of our

group have been involved in this process from the early beginnings, like autotuning for electron microscopy (Koster et al. 1987), to an extension of the same approach for tilted samples (presented in chapter 3 of this publication; Ziese et al, 2002c) and the work about pre-calibration tomography that considerably speeds up data acquisition (chapter 2; Ziese et al, 2002).

Presently, the developments have evolved to a point were the main interest in tomography with transmission electron microscopy shifts from methodic or technical investigations, like e.g. the value of high voltage or energy filtering (Grimm et al., 1997) for thick samples, to the realization that the next big step towards the widespread application will be made in the field of image processing. Software for 3D reconstructions from tomographic data series, developed in specialized laboratories like e.g. IMOD, Boulder Laboratory for 3D Fine Structure or IVE, Macromolecular Structure Group, UCSF, certainly take account of necessary aspects of the reconstruction process, but could be characterized as still being in a 'homegrown' state, that certainly does not appeal to non-experts. A recent congress on electron microscopy (ICEM 15) displayed first attempts of software suppliers (JEOL Ltd., Tietz GmbH) to provide programs that guide inexperienced users through the reconstruction progress—but the commercial availability of robust programs for the 3D reconstruction of any kind of sample, including marker-less alignment, still seems to lie in the near future.

Another challenge in the widespread application of electron tomography that has to be dealt with is the difficulty provided by the interpretation of 3D reconstructions (tomograms). While the results of single particle analysis can readily be displayed as surface rendered maps, the depiction of the volumetric information contained in tomograms remains problematic. Showing single slices of the reconstruction is of course a lossless method, but one 'cannot see the wood for the trees', especially when there are only modest contrast differences in the sample that prohibit thresholding. Volume rendering emphasizes a bit more the 3D structure, but otherwise suffers the same problem. As a result most investigators have mainly used software for hand-drawing outlines of interesting structures inside tomograms. Examples for single-slice (Figs. 7A and 7C), surface-rendered (Figs. 7B and 7D) and modelled (Fig. 8B) representations of tomograms can be found in chapter 2. Recently, there are trends in

the development of methods for automated segmentation (see special issue of *JSB*, 138, 2002).

Examples for other aspects of computer science that will influence and facilitate electron microscopy and thus electron tomography in the near future are remote (tele) microscopy and distributed computing/grid services (see e.g. Voelkl et al., 1998; Hadida-Hassan et al., 1999). Both approaches revolve around the idea that specialized resources (like high-voltage electron microscopes) might not be available locally to all investigators and should thus be shared over fast (inter)national computer networks. The investigation of dangerous material under security containment (like e.g. infectious particles) also benefits from the advances in the area of remote microscopy.

While electron tomography has matured and become an established method and a commercially available product in the biological sciences, the field of materials sciences has only discovered it during the last few years. While we have shown that transmission electron tomography can be useful in the investigation of zeolite crystals (see addendum to chapter 2), others provided evidence that HAADF-STEM tomography can be an outcome for high-resolution work on crystalline samples (Midgley et al. 2001) and a combination of electron energy loss spectroscopy with transmission electron tomography can yield insight into element distributions in samples (Weyland and Midgley 2001). Vice versa, investigations in the materials sciences have impact on biological applications, as we have re-adopted the technique to show that HAADF-STEM tomography can be useful for the 3D localization of ultrasmall gold labels in cell sections (chapter 4; Ziese et al., 2002b). This can become valuable in the determination of functions and interactions of proteins, as addressed in the field of cell dynamics and proteomics.

References

Alfredsson, V., Ohsuna, T., Terasaki, O. and Bovin, J.-O. 1993. Investigation of the surface structure of the zeolites FAU and EMT by high-resolution transmission electron microscopy. *Angew. Chem., Int. Ed. Engl.* 32: 1210-1213.

Baba, N., Terayama, K., Yoshimizu T., Ichise, N., and Tanaka, N. (2001) An auto-tuning method for focusing and astigmatism correction in HAADF-STEM, based on the image contrast transfer function. *J. Electron Microsc.* 50: 163-176.

Baumeister, W., and A.C. Steven. 2000. Macromolecular electron microscopy in the era of structural genomics. *Trends in Biochemical Sciences* 25(12): 624-631.

Baumeister, W., Grimm, R., and J. Walz. 1999. Electron tomography of molecules and cells. *Trends Cell Biol.* 9(2): 81-85.

Beorchia, A., Heliot, L., Menager, M., Kaplan, H., and D. Ploton. 1993. Applications of medium voltage STEM for the 3-D study of organelles within very thick sections. *J. Microsc.* 170(3): 247-258.

Bonfanti, L., A.A. Mironov, Jr., J.A. Martinez-Menarguez, O. Martella, A. Fusella, M. Baldassarre, R. Buccione, H.J. Geuze, A.A. Mironov, and A. Luini. 1998. Procollagen traverses the Golgi stack without leaving the lumen of cisternae: evidence for cisternal maturation. *Cell.* 95: 993–1003.

Braunfeld, M.B., Koster, A.J., Sedat, J.W., and D.A. Agard. 1994. Cryo automated electron tomography: towards high-resolution reconstructions of plastic-embedded structures. *J. Microsc.* 174(2): 75-84.

Carragher, B., Kisseberth, N., Kriegman, D., Milligan, R.A., Potter, C.S., Pulokas, J., and A. Reilein. 2000. Leginon: An automated system for acquisition of images from vitreous ice specimens. *J. Struct. Biol.* 132(1): 33-45.

Choi-Feng, C., Hall, J. B., Huggins, B. J. and Beyerlein, R. A. 1993. Electron microscope investigation of mesopore formation and aluminum migration in USY catalysts. *J. Catal.* 140: 395-405.

Corma, A., Fornes, V., Pergher, S. B., Maesen, Th. L. M. and Buglass J. G. 1998. Delaminated zeolite precursors as selective acidic catalysts. *Nature* 396: 353-356.

Creyghton, E. J., Elings, J. A., Downing, R. S., Sheldon, R. A. and van Bekkum, H. 1996. New multifunctional probe for testing outer surface activity of zeolites: application to surface-located platinum clusters and acid sites. *Microporous Mater. 5*: 299-307.

Crowther, R.A., DeRosier, D.J., and A. Klug. 1970. The reconstruction of a three-dimensional structure from its projections and its application to electron microscopy. *Proc. R. Soc. Lond.* (A) 317: 319-340.

Danscher, G. (1981) Histochemical demonstration of heavy metals. A revised version of the silver method suitable for both light and electron micorscopy. *Histochemistry* 71: 1-16.

DeRosier, D.J., and A. Klug. 1968. Reconstruction of threedimensional structures from electron micrographs. *Nature* 217: 130-134.

Dierksen, K., Typke, D., Hegerl, R., Walz, J., Sackmann, E., and W. Baumeister. 1995. Three dimensional structure of lipid vesicles embedded in vitreous ice and investigated by automated electron tomography. *Biophys. J.* 68(4): 1416-1422.

Dierksen, K., Typke, D., Hegerl, R., and W. Baumeister. 1993. Towards automatic electron tomography. II. Implementation of autofocus and low-dose procedures. *Ultramicroscopy* 49: 109-120.

Dierksen, K., Typke, D., Hegerl, R., Koster, A.J., and W. Baumeister. 1992. Towards automatic electron tomography. *Ultramicroscopy* 40: 71-87.

Frank, J., Radermacher, M., Penczek, P., Ahu, J., Li, Y., Ladjadj, M., and A. Leith. 1996. SPIDER and WEB: processing and visualization of images in 3D electron microscopy and related fields. *J. Struct. Biol.* 116: 190-199.

Frank, J. 1995. Approaches to large-scale structures. *Curr. Opin. Struct. Biol.* 5(2): 194-201.

Frank, J. 1992. Electron Tomography. Plenum Press. New York.

Freyhardt, C. C., Tsapatsis, M., Lobo, R. F., Balkus, K. J., Jr. and Davis, M. E. 1996. A high-silica zeolite with a 14-tetrahedral-atom pore opening. *Nature* 295: 295-298.

Fung, J.C., Liu, W., de Ruijter, W.J., Chen, H., Abbey, C.K., Sedat, J.W., and D.A. Agard. 1996. Toward fully automated high-resolution electron tomography. *J. Struct. Biol.* 116(1): 181-189.

Geerts, W.J.C., Burger K.N., Mironov A.A. and Koster A.J. 2002, personal communication, unpublished results.

Grimm, R., Singh, H., Rachel, R., Typke, D., Zillig, and W. Baumeister. 1998. Electron tomography of ice-embedded prokaryotic cells. *Biophys. J.* 74(2 Pt 1): 1031-1042.

Grimm, R., Barmann, M., Hackl, W., Typke, D., Sackmann, E., and W. Baumeister. 1997. Energy filtered electron tomography of ice-embedded actin and vesicles. *Biophys. J.* 72(1): 482-489.

Guckenberger, R.(1982) Determination of a common origin in the micrographs of tilt series in three-dimensional electron microscopy. *Ultramicroscopy* 9: 167-174.

Hadida-Hassan M., Young S.J., Peltier S.T., Wong M., Lamont S. and Ellisman M.H. 1999. Web-based telemicroscopy. *J Struct Biol* 125(2-3): 235-45.

Hainfeld, J.F., and Powell,R.D. (2000) New Frontiers in Gold Labeling. *J. Histochem. Cytochem.* 48: 471-480.

Hainfeld, J.F., Powell, R.D., Stein, J.L., Hacker, G.W., Hauser-Kronberger, C., Cheung, A., and Schöfer, C. 1999. Gold-based autometallography. in Bailey, G.W., Jerome, W.G., McKernan, S., Mansfield, J.F., Price, R.L. (eds) Proc. 57th Ann. Mtg., Microsc. Soc. Am. Springer, Berlin, Heidelberg, New York, 486-487.

Hainfeld, J.F. 1990. STEM analysis of Janssen Aurooprobe One. in Bailey G. (Ed), Proc XIIth Int Congr Electron Microsc. San Francisco, San Francisco Press, 954-955.

Hart, R. 1968. Electron microscopy of unstained biological material: The polytropic montage. *Science* 159: 1464-1467.

van Heel M., Harauz G. and Orlova E.V. 1996. A new generation of the IMAGIC image processing system. *J. Struct. Biol.* 116(1):17-24.

Hegerl, R., and A. Altbauer. 1982. The "EM" program system. *Ultramicroscopy* 9(1-2): 109-116.

Hegerl, R. and Hoppe, W. 1976. Influence of electron-noise on three-dimensional image reconstruction. Z. Naturforsch. 31a: 1717-1721.

Hoppe, W., Hegerl, R. 1980. Three-dimensional structure determination by electron microscopy (nonperiodic specimens), in Computer processing of electron microscope images, ed. By P.W. Hawkes, Springer, Berlin, Heidelberg pp. 127-185.

Hoppe W., Schramm, H.J., Sturm, M., Hunsmann, N., Gassmann, J. 1976. Three-dimensional electron microscopy of individual biological objects. Part I. Methods. Z. Naturforsch. 31a: 645-655.

Hoppe, W., Langer, R., Knesch, G., and Ch. Poppe. 1968. Proteinkristalstruktur-analyse mit Elektronenstrahlen. *Naturwissenschaften* 5: 333-336.

Hudspeth, A.J. 1997. How Hearing Happens. Neuron 19: 947-950.

Humbel, B.M., de Jong, M.D., Muller, W.H., and A.J. Verkleij. 1998. Pre-embedding immunolabeling for electron microscopy: an evaluation of permeabilization methods and markers. *Microsc. Res. Tech.* 42(1): 43-58.

Janssen, A.H., van der Voort, P., Koster, A.J. and de Jong, K.P. A 3D-TEM study of the shape of mesopores in SBA-15 and modified SBA-15 materials. *Chem. Commun*., 2002: 1632–1633.

Janssen, A.H., Koster, A.J., and K.P. de Jong. 2001. Three-dimensional transmission electron microscopic observations of mesopores in dealuminated zeolite Y. *Angewandte Chemie International Edition* 40(6): 1102-1104.

Koster, A.J., Ziese, U., Verkleij, A.J., Janssen, A.H., and K.P. de Jong. 2000. Three-Dimensional Transmission Electron Microscopy: A Novel Imaging and Characterization Technique with nanometer Scale Resolution for Material Science. *Phys. Chem. B*:104: 9368-9370.

Koster, AJ., Grimm, R., Typke, D., Hegerl, R., Stoschek, A., Walz, J., and W. Baumeister. 1997. Perspectives of molecular and cellular electron tomography. *J. Struct. Biol.* 120(3): 276-308.

Koster, A.J., Chen, H., Sedat, J.W., and D.A. Agard. 1992. Automated microscopy for electron tomography. *Ultramicroscopy* 46(1-4): 207-227.

Koster, A.J., de Ruiter, W.J., van den Bos, A., and K.D. van der Mast. 1989. Autotuning of a TEM using minimum dose. *Ultramicroscopy* 27: 251-72.

Koster, A.J., Van den Bos, A., and K.D. van der Mast. 1987. An autotuning method for a TEM. *Ultramicroscopy* 21: 209-222.

Kremer, J.R., Mastronarde, D.N., and J.R. McIntosh. 1996. Computer Visualization of Three-Dimensional Image Data Using IMOD. *J. Struct. Biol.* 116: 71-76.

Ladinsky, M.S., D.N. Mastronarde, J.R. McIntosh, K.E. Howell, and L.A. Staehelin. 1999. Golgi structure in three dimensions: functional insights from the normal rat kidney cell. *J. Cell Biol.* 144: 1135–1149.

Maschmeyer, T., Rey, F., Sankar, G. and Thomas, J. M. 1995. Heterogeneous catalysts obtained by grafting metallocene complexes onto mesoporous silica. *Nature* 378: 159-162.

McEwen, B.F., and M. Marko. 2001. The emergence of electron tomography as an important tool for investigating cellular ultrastructure. *J. Histochemistry & Cytochemistry* 49(5): 553-563.

McEwen, B.F., and M. Marko. 1999. Three-dimensional electron microscopy and its application to mitosis research. *Methods Cell Biol.* 61: 81-111.

McEwen, B.F., Downing, K.H., and R.M. Glaeser. 1995. The relevance of dose-fractionation in tomography of radiation-sensitive specimens. *Ultramicroscopy* 60: 357-373.

Meima, G. R. 1998. Advances in cumene production. *Cattech* 2: 5-12.

Midgley, P.A., Weyland M., Meurig Thomas J. and Johnson B.F.G. Z-Contrast tomography: a technique in three-dimensional nanostructural analyis based on Rutherford scattering. *Chem. Commun.*, 2001: 907-908.

Mintova, S., Olson, N. H., Valtchev, V. and Bein, T. 1999. Mechanism of zeolite A nanocrystal growth from colloids at room temperature. *Science* 283: 958-960.

Mironov, A.A., Beznoussenko, G.V., Nicoziani, P., Martella, O., Trucco, A., Kweon, H.S., Di Giandomenico, D., Polishchuk, R.S., Fusella, A., Lupetti, P., Berger, E.G., Geerts, W.J., Koster, A.J., Burger, K.N., Luini, A. 2001. Small cargo proteins and large aggregates can traverse the Golgi by a common mechanism without leaving the lumen of cisternae. *J Cell Biol.* 24: 155(7):1225-38.

Polishchuk, R.S., E.V. Polishchuk, P. Marra, S. Alberti, R. Buccione, A. Luini, and A.A. Mironov. 2000. Correlative light-electron microscopy reveals the tubular-saccular ultrastructure of carriers operating between Golgi apparatus and plasma membrane. *J. Cell Biol.* 148: 45–58.

Potter, C.S., Chu, H., Frey, B., Green, C., Kisseberth, N., Madden, T.J., Miller, K.L., Nahrstedt, K., Pulokas, J., Reilein, A., and others. 1999. Leginon: a system for fully automated acquisition of 1000 electron micrographs a day. *Ultramicroscopy* 77(3-4): 153-161.

Pulokas, J., Green, C., Kisseberth, N., Potter, C.S., and B. Carragher. 1999. Improving the positional accuracy of the goniometer on the Philips CM series TEM. *J. Struct. Biol.* 128(3): 250-256.

Radermacher, M. 1992. Weighted back-projection methods. in *Electron Tomography*. Frank, J. (Ed), Plenum Press, New York, 91-115.

Radon, J. 1917. Uber die Bestimmung von Funktionen durch ihre Integralwerte langs gewisser Mannigfaltigkeiten. Berichte uber die Verhandlungen der Koniglich Sachsischen gesellschaft der Wissenschaften zu Leibzig. *Math. Phys. Klasse*, 69: 262-277.

Rath B.K., Marko M., Radermacher M., and J. Frank. 1997. Low-dose automated electron tomography: a recent implementation. *J. Struct. Biol.* 120(3): 210-218.

Reimer, L. (1997) Electron-Probe Broadening by Multiple Scattering in Transmission Electron Microscopy. 4th edition, Springer-Verlag, Berlin, 191-194.

Rothman, J.E., and F.T. Wieland. 1996. Protein sorting by transport vesicles. *Science.* 272: 227–234.

Sasaki, Y., Suszuki, T., Takamura, Y., Saji, A. and Saka, H. 1998. Structure analysis of the mesopore in dealuminated zeolite Y by high resolution TEM observation with slow scan CCD camera. *J. Catal.* 178: 94-100.

Sasaki, Y., Suzuki, T. and Ikuhara, Y. 1995. Direct observation of channel srtuctures in zeolite A with a slow scan charge-coupled-device camera. *J. Am. Ceram. Soc.* 78: 1411-1413.

Schroeter J.P., and J.P. Bretaudiere. 1996. SUPRIM: easily modified image processing software. *J. Struct. Biol.* 116: 131-137.

Starink J., Humbel B., and A.J. Verkleij. 1995. Three-dimensional localization of immunogold markers using two tilted electron microscope recordings. *Biophys. J.* 68(5): 2171-2180.

Stierhoff, Y.D., Humbel, B.M., Homann, R., Otten, M.T., and Schwarz, H. 1992. Direct visualization and silver enhancement of ultra-small gold tagged antibodies on immunolabelled ultrathin resin sections. *Scanning Microsc.* 6: 1009-1022.

Tokuyasu, K.T. 1973. A technique for ultracryotomy of cell suspensions and tissues. *J. Cell Biol.* 57: 551-565.

Verkleij, A.J., Koster, A.J., Müller, W.H., and Humbel, B.M. 1999. Immuno-Gold Labeling in Transmission Electron Microscopy. in *Molecular Mechanisms of Transcellular Signaling*, Thiery, J.P. (Ed), IOS Press.

Voelkl E., Alexander, K.B., Mabon, J.C., O'Keefe, M.A., Postek, M.T., Wright M.C. and Zalzuzec, N.J. 1998. *Proc. XIVth Int. Congress for Electron Microscopy* **1,** 289-290.

Weyland M. and Midgley, P.A. 2001. Three Dimensional Energy Filtered Transmission Electron Microscopy (3D-EFTEM). *Microsc. Microanal. 7 (Suppl 2: Proceedings).* 1162-1163.

Ziese U., Geerts W.J.C., van der Krift T., Verkleij A.J. and Koster A.J. 2002c. Correction of autofocusing errors due to specimen tilt. *J Microsc.* Accepted after revision.

Ziese, U., Kübel, C., Verkleij, A.J. and Koster, A.J. 2002b. Three-dimensional localization of ultrasmall immuno-gold labels by HAADF-STEM tomography. *J Struct Biol.* 138(1-2): 58-62.

Ziese, U., Janssen, A.H., Murk, J.L., Geerts, W.J.C., Krif,t T., Verkleij, A.J., and Koster, A.J. 2002 Automated high-throughput electron tomography by pre-calibration of image shifts. *J. Microscopy* 205(2): 187-200.

Publications

Ziese, U., Geerts, W.J.C., van der Krift, T., Verkleij, A.J. and Koster, A.J. 2002c. Correction of autofocusing errors due to specimen tilt. *J. Microsc.* Accepted after revision.

Ziese, U., Kübel, C., Verkleij, A.J. and Koster, A.J. 2002b. Three-dimensional localization of ultrasmall immuno-gold labels by HAADF-STEM tomography. *J. Struct. Biol.* 138(1-2): 58-62.

Baldock, C., Gilpin, C., Koster, A., **Ziese, U.**, Kadler, K., Kielty, C. and Holmes, D. 2002. Three-dimensional reconstructions of extracellular matrix polymers using automated electron tomography. *J. Struct. Biol.* 138(1-2): 130.

Ziese, U., Janssen, A.H., Murk, J.L., Geerts, W.J., van der Krift, T., Verkleij, A.J. and Koster, A.J. 2002. Automated high-throughput electron tomography by pre-calibration of image shifts. *J. Microsc.* 205(Pt 2): 187-200.

Holmes, D.F., Gilpin, C.J., Baldock, C., **Ziese, U.**, Koster, A.J. and Kadler, K.E. 2001. Corneal collagen fibril structure in three dimensions: Structural insights into fibril assembly, mechanical properties, and tissue organization. *Proc. Natl. Acad. Sci. USA.* 98(13): 7307-12.

Baldock, C., Koster, A.J., **Ziese, U.**, Rock, M.J., Sherratt, M.J., Kadler, K.E., Shuttleworth, C.A. and Kielty, C.M.R. 2001. The supramolecular organization of fibrillin-rich microfibrils. *J. Cell Biol.* 152(5): 1045-56.

Koster, A.J., **Ziese, U.**, Verkleij, A.J., Janssen, A.H. and de Jong, K.P. 2000. Three-dimensional transmission electron microscopy: A novel imaging and characterization technique with nanometer scale resolution for materials science. *J. Phys. Chem. B* 104: 9368-9370.

Koster, A.J., **Ziese, U.**, Verkleij, A.J., Janssen, A.H., de Graaf, J., Geus, J.W. and de Jong, K.P. 2000. Development and Application of 3-Dimensional Transmission Electron Microscopy (3D-TEM) for the Characterization of Metal-Zeolite Catalyst Systems. *Stud. Surf. Sci. Catal.* 130: 329.

Muller, W.H., Koster, A.J., Humbel, B.M., **Ziese, U.**, Verkleij, A.J., van Aelst, A.C., van der Krift, T.P., Montijn, R.C. and Boekhout, T. 2000. Automated electron tomography of the septal pore cap in Rhizoctonia solani. *J. Struct. Biol.* 131(1): 10-8.

Arnold, H.P., **Ziese, U.** and Zillig, W. 2000. SNDV, a novel virus of the extremely thermophilic and acidophilic archaeon Sulfolobus. *Virology* 272(2): 409-416.

Arnold, H.P., Zillig, W., **Ziese, U.**, Holz, I., Crosby, M., Utterback, T., Weidmann, J.F., Kristjanson, J.K., Klenk, H.P., Nelson, K.E. and Fraser, C.M. 2000. A novel lipothrixvirus, SIFV, of the extremely thermophilic crenarchaeon Sulfolobus. *Virology* 267(2): 252-266.

Brok, R., van Gelder, P., Winterhalter, M., **Ziese, U.**, Koster, A.J., de Cock, H., Koster, M., Tommassen, J. and Bitter, W. 1999. The C-terminal domain of the Pseudomonas secretin XcpQ forms oligomeric rings with pore activity. *J. Mol. Biol.* 294(5): 1169-1179.

Prangishvili, D., Arnold, H.P., Gotz, D., **Ziese, U.**, Holz, I., Kristjansson, J.K., Zillig, W. 1999. A novel virus family, the Rudiviridae: Structure, virus-host interactions and genome variability of the sulfolobus viruses SIRV1 and SIRV2. *Genetics* 152(4): 1387-1396.

Offner, S., **Ziese, U.**, Wanner, G., Typke, D., Pfeifer, F. 1998. Structural characteristics of halobacterial gas vesicles. *Microbiology* 144 (Pt 5): 1331-1342.

Curriculum Vitae

Ulrike Ziese werd op 18 september 1966 in Dortmund (Duitsland) geboren. In 1986 behaalde zij het diploma "Allgemeine Hochschulreife" aan het Helmholtz Gymnasium in Dortmund. Aansluitend startte zij met de studie "Physik" (natuurkunde) aan de Universität Dortmund en behaalde in 1992 het diploma "Physikerin" (doctoraal examen natuurkunde) met als specialisatierichtingen "Elektronik", "Beschleuniger" (deeltjes versneller) en "Informatik". De volgende 5 jaar heeft zij aan het Max-Planck Institut für Biochemie, Martinsried (Duitsland) onder leiding van Dr. D. Typke en Prof. Dr. W. Baumeister aan cryo-applicaties in de elektronenmicroscopie gewerkt. In july 1998 begon ze als onderzoeker aan de Universiteit Utrecht bij de vakgroep Moleculaire Celbiologie onder leiding van Dr. Ir. A.J. Koster en Prof. Dr. A. J. Verkleij. Gedurende deze periode heeft ze onder andere aan het in deze proefschrift beschreven onderzoek gewerkt.

Samenvatting

Elektronentomografie is een methode om drie-dimensionale (3D) structurele informatie uit elektronenmicroscopische opnames te verkrijgen. Het kan worden toegepast op een grote verscheidenheid van preparaten die voor transmissie elektronenmicroscopie (TEM) geschikt zijn. Voorbeelden van preparaten van biologische oorsprong zijn plakjes van cellen en weefsel (tot 500 nm dik). Voorbeelden van materiaalkundige oorsprong zijn zeoliet kristallen, polymeren en elektronische bouwdelen voor halfgeleiders.

Het grote voordeel van elektronentomografie boven andere methoden met nm-resolutie (zoals *angular reconstitution*, nucleaire magnetische resonantie spectroscopie (NMR), elektronenkristallografie en Röntgen-kristallografie) is dat het niet nodig is om (a) over eenheidscellen of deeltjes te middelen of (b) structurele symmetrie aanwezig in de preparaten uit te moeten buiten. Elektronentomografie kan dus worden toegepast op unieke structuren—met als enige beperking dat het geregistreerde beeldcontrast in het elektronenmicroscopische beeld een projectie is van een fysische eigenschap van het preparaat, bijvoorbeeld zijn massa/elektronen dichtheid. Dit impliceert dat in de elektronentomografie naast conventionele helderveld transmissie-elektronenmicroscopie, ook energie filtering (*zero-loss* of element specifiek) of *high angular annular dark-field* (HAADF) scanning transmissie elektronenmicroscopie (STEM) toegepast kan worden.

Data opname voor elektronentomografie kan als een soort super-stereografie beschouwd worden. In plaats van dat er slechts twee beelden onder verschillende kijkhoeken opgenomen worden, kan een tomografische data set bestaan uit meer dan 151 beelden, gemaakt over een hoekbereik van 150°. Hoe meer beelden, en hoe groter het kantelingsbereik, des te beter zal de resolutie van de 3D-reconstructie zijn. Een ruwe schatting van de haalbare resolutie in een 3D-reconstructie kan gemaakt worden door drie keer de doorsnede van het preparaat te delen door het aantal beelden dat opgenomen wordt (voor nauwkeurige berekeningen Radermacher, 1992). Voor een 300 nm dik preparaat zou dit met 151 beelden een resolutie van 6 nm betekenen. De theorie voor de 3D-reconstructie uit projecties (*weighted backprojection*,

inverse radon transform) bestaat al honderd jaar (Radon, 1917) en de eerste toepassingen op elektronenmicropische beelden zijn zo'n 30 jaren geleden gepubliceerd (DeRosier and Klug, 1968). Echter, de technische eisen die met het opnemen van zoveel beelden verbonden zijn, namelijk de rotatie van de preparaathouder en het centreren en focusseren van het interessante gebied voor iedere opname, hebben de routinematige toepassing van de techniek voor het 3D-onderzoek met nm-resolutie voor lange tijd geremd. Een van de redenen waardoor de elektronentomografie in de loop van het laatste decennium meer toegepast wordt (Dierksen et al., 1992; Koster et al., 1992) ligt in de beschikbaarheid van digitale gevoelige slow-scan CCD cameras voor de data opname, snellere computer systemen gekoppeld aan de electronenmicroscopen voor on-line beeldverwerking, en software bestuurbare elektronenmicroscopen. Onder deze omstandigheden konden automatische systemen voor de elektronentomografische data opname ontwikkeld worden—en de methode zelfs geschikt maken voor onderzoek aan de meest stralings gevoelige preparaten, zoals bijvoorbeeld *frozen-hydrated* materiaal (Dierksen et al., 1993 and 1995).

Ook al hebben bovengenoemde ontwikkelingen de toepassing van de elektronen-tomografie op een grote hoeveelheid verschillende preparaten mogelijk gemaakt, toch heeft de hoeveelheid tijd en expertise die nodig waren om een kantel-serie op te nemen (meerdere uren) vele potentiële gebruikers afgeschrikt om de methode routinematig te gebruiken. In het tweede hoofdstuk beschrijven wij een methode voor geautomatiseerde elektronentomografische data opname die de benodigde tijd met een faktor vijf reduceert en zo de data opname in minder dan een uur mogelijk maakt (Ziese et al, 2002). De methode bevat een pre-calibratie stap—meting en correctie van beeld verschuivingen en defocus veranderingen bij een lage vergroting om verplaatsingen oplopend tot enkele μm te detecteren—die vóór de eigenlijke beeld opname toegepast wordt. Deze stap maakt het overbodig om tijdens de data opname tussen hoge en lage vergrotingen heen en weer te schakelen, wat een heel tijdrovende procedure is vanwege de noodzakelijke stabiliseringen van de electro-magnetische lenzen. De methode is erop gebaseerd dat de beeld verschuivingen veroorzaakt worden door (a) een niet-eucentrische plaatsing van het preparaat en (b) het niet-overeenkomen van de optische-as met de kantel-as van de preparaathouder. Door het

mathematisch modeleren van de preparaat beweging, zijn de bewegingen preparaat onafhankelijk en vrijwel geheel voorspelbaar.

Pre-calibratie elektronentomografie wordt in ons laboratorium nu sinds twee jaar routinematig gebruikt. Intussen is de methode zelfs een geïntegreerd onderdeel van meerdere commerciële software pakketten voor geautomatiseerde tomografie (Emispec, Inc., Tempe, US; FEI Co. Eindhoven; TVIPS, GmbH, Gauting, Duitsland). Het addendum behorend bij hoofdstuk 2 geeft voorbeelden voor de toepassing van de methode met een materiaalkundig en een biologisch preparaat. Het eerste voorbeeld laat zien dat het 3D-morfologische onderzoek aan zeolieten, welke belangrijke materialen zijn voor katalytische applicaties zoals *hydro-isomerization* van alkanen en *hydrocracking* van zware aardolie fracties, een beter begrip kan opleveren voor de katalytische activiteit en selectiviteit van deze materialen. Het tweede voorbeeld illustreert met de 3D-studie aan het Golgi complex dat elektronentomografie van met hoge druk ingevroren en *freeze-substituted* coupes van celorganellen kan helpen bij het onderzoek aan celdynamiek en *proteomics*.

In hoofdstuk 3 wordt een methode besproken voor de correctie van autofocuserings fouten als gevolg van gekantelde preparaten (Ziese et al., 2002c). Dit onderwerp is van belang omdat gekantelde preparaten een precieze voorspelling van defocus, met bijvoorbeeld de pre-calibratie tomografie, onmogelijk kan maken. De defocus meting met behulp van de gekantelde bundel methode kan—vanwege een defocus variatie in ieder beeld—problemen opleveren als deze bij lage vergrotingen en hoge kantel-hoeken toegepast wordt. De methode voor de juiste kruis correlatie (XCF) van twee beelden van een gekanteld preparaat, opgenomen met verschillende bundel kantelingen is een modificatie van de *cosinus stretch*, die toegepast wordt bij het uitlijnen van beelden die met verschillende preparaat kantelingen opgenomen zijn.

De elektronentomografie is niet beperkt tot toepassing voor helderveld transmissie elektronenmicroscopie. Data opname in HAADF-STEM modus maakt de methode ook bruikbaar voor bijvoorbeeld kristallijne monsters, die niet in TEM modus kunnen worden opgenomen, omdat dergelijke preparaten kantelhoek afhankelijke reflecties vertonen (Bragg reflecties). Nadat voor kristallijn materiaal aangetoond was dat insluitingen met een grootte van maar één nm te detecteren zijn (Midgely et al, 2001), hebben wij deze benadering toegepast voor de detectie van ultra kleine

immuno goud markeringen, geabsorbeerd op met zware metalen gekleurde coupes van biologisch materiaal. De eerste experimenten, die in hoofdstuk 4 beschreven worden (Ziese et al., 2002b), laten zien dat HAADF-STEM elektronentomografie een zeer nuttige techniek kan zijn bij de nauwkeurige 3D immuno-lokalisatie van eiwitten. Tot nu toe is de toepassing van deze methode tijdrovend omdat alle HAADF-STEM beelden handmatig opgenomen moeten worden. Wij gaan er echter van uit dat pre-calibratie elektronentomografie een bijdrage kan leveren aan de automatisering van data opname en dus ook aan de routinematige toepassing van STEM.

Tenslotte, wordt in hoofdstuk 5 het werk samengevat en bediscussieerd met betrekking tot recente ontwikkelingen in de automatisering en toepassing van de elektronentomografie.

…

Printed by Shaker Verlag GmbH, Aachen, Germany, www.shaker.de.

Als je in Duitsland het boekje aan jouw collega's uitdeelt, is het de gewoonte dat je daar op de eerste pagina voor een aantal mensen wat persoonlijke opmerkingen plaast. Het mooiste wat ik zelf gekregen heb toen ik in Duitsland werkte was zo iets als "als je op dit boekje stapt wordt je groter". Ik zou de waarde van een proefschrift niet beter met eigen woorden kunnen karakteriseren.

Waar ik heel veel van genoten heb is het werken in onze afdeling, waar iedereen de mogelijkheid heeft naar eigen interesse en vermogen bij te dragen aan de ontwikkeling van wetenschap. Arie, Bram van harte bedankt dat jullie niet opgegeven hebben mijn interesse voor het spelen met mooie technische apparatuur in een productieve richting te begeleiden.

Ook wil ik vooral diegenen bedanken die onze microscopie afdeling op de een of andere manier aan het runnen houden en op deze manier het onderzoek mogelijk maken.

Tenslotte nog dank aan allen die met discussies, proeflezen, editeren of andere hulp bijgedragen hebben aan HET WERK.

Hartelijk dank dus aan Antje, Arie, Bram, Chris, Christian, Gonneke, Hans, Henk, Jean-Luc, Koert, Ries, Theo, Wally, Willie, ...

Ulrike Ziese